Titre: Title:	Fluoroscopic navigation to guide RF catheter ablation of cardiac arrhythmias
Auteur: Author:	Pascal Fallavollita
Date:	2004
Type:	Mémoire ou thèse / Dissertation or Thesis
Référence: Citation:	Fallavollita, P. (2004). Fluoroscopic navigation to guide RF catheter ablation of cardiac arrhythmias [Mémoire de maîtrise, École Polytechnique de Montréal]. PolyPublie. https://publications.polymtl.ca/7480/

URL de PolyPublie: PolyPublie URL:	https://publications.polymtl.ca/7480/
Directeurs de recherche: Advisors:	Pierre Savard
Programme: Program:	Non spécifié

NOTE TO USERS

UNIVERSITÉ DE MONTRÉAL

FLUOROSCOPIC NAVIGATION TO GUIDE RF CATHETER ABLATION OF CARDIAC ARRHYTHMIAS

PASCAL FALLAVOLLITA
INSTITUT DE GÉNIE BIOMEDICAL
ÉCOLE POLYTECHNIQUE DE MONTRÉAL

MÉMOIRE PRÉSENTÉ EN VUE DE L'OBTENTION
DU DIPLÔME DE MAÎTRISE EN SCIENCES APPLIQUÉES
(GÉNIE BIOMEDICAL)
AOÛT 2004

Library and Archives Canada

Published Heritage Branch

395 Wellington Street
Ottawa ON K1A 0N4
Canada

Bibliothèque et Archives Canada

Direction du Patrimoine de l'édition

395, rue Wellington
Ottawa ON K1A 0N4
Canada

Your file Votre référence
ISBN: 0-612-97947-4
Our file Notre référence
ISBN: 0-612-97947-4

UNIVERSITÉ DE MONTRÉAL

ÉCOLE POLYTECHNIQUE DE MONTRÉAL

Ce mémoire intitulé:

FLUOROSCOPIC NAVIGATION TO GUIDE
RF CATHETER ABLATION OF CARDIAC ARRHYTHMIAS

présenté par: FALLAVOLLITA Pascal
en vue de l'obtention du diplôme de: Maîtrise ès sciences appliquées
a été dûment acceptée par le jury d'examen constitué de:

M. VINET Alain, Ph.D., président
M. SAVARD Pierre, Ph.D., membre et directeur de recherche
Mme CHERIET Farida, Ph.D., membre

La science cherche le mouvement perpétuel. Elle l'a trouvé: c'est elle-même.

Victor Hugo

ACKNOWLEDGEMENTS

I would like to thank my research director, Professor Pierre Savard, for his constant support and his valuable suggestions that helped me throughout this work. He gave me the freedom to do my work independently and his availability and capacity to answer all questions are quite fascinating. I also extend my gratitude to him for allowing me to present my work at the *26th Annual International Conference IEEE Engineering in Medicine and Biology Society* at San Francisco. This master's research couldn't have been made possible without his support.

I would like to thank the members at l'Hôpital Sacré Coeur de Montréal, for their help and encouragement during the realization of this work. My gratitude to : Gilberto Sierra, Bruno Dubé, Pierre Roque, Gaétan Tremblay, le Professeur Alain Vinet, le Professeur Robert LeBlanc, Maryline de Chantal, Louis-Philippe Richer, Philippe Comptois, Simon Corbeil-Letourneau, Jean-Yves Domerçant, Pierre Fortier et Caroline Bouchard.

Finally, I'd like to thank all my friends that have supported me and in particular to my parents who have always encouraged me to face adversity and surmount any obstacles in my way, and for having taught me certain principles that will guide me throughout the remainder of my life.

ABSTRACT

Severe disorders of the cardiac rhythm that can cause syncope or sudden cardiac death can be treated by radio-frequency (RF) catheter ablation. The precise localization of the arrhythmogenic site and the positioning of the RF catheter over that site are problematic as they impair the efficiency of the procedure and are time consuming.

Three different commercial systems that provide a 3D color display of the cardiac electrical activation sequence have been developed recently to facilitate the mapping of complex arrhythmias, however they are quite costly. Our group is attempting to develop a more affordable fluoroscopic navigation system. Preliminary results have shown that it is possible to effectively superimpose over a fluoroscopic X-ray image of the heart, an isochronal map depicting the cardiac electrical activation sequence that is generated from geometrical data obtained from fluoroscopic images of the catheters. However, initial attempts in extracting 3D information, such as the depth of an electrode within the heart chamber, from monoplane images were inconclusive. The main objective of this work has been to continue perfecting our three-dimensional mapping system using data obtained from an animal experiment.

Biplane analysis: the three-dimensional coordinates of a mapping catheter that was positioned at different sites in the left ventricle were obtained from two perpendicular fluoroscopic images. A 3D Convex Hull was used to organize the electrical and geometrical data: each node of the Convex Hull was associated with the electrical activation time (in ms) measured with the catheter at one location over the endocardial surface. The activation time was represented by a color code that was linearly interpolated onto the Convex Hull: red signifying early activation times and blue associated with the latest activation times. A 2D isochronal map was then generated by retaining the nodes of the triangles constituting the Convex Hull whose normals were visible from a certain point of view (for example, we retained activation times associated with normals pointing in the –Y direction to create a map for the left lateral view). The isochronal map was then superimposed over its associated fluoroscopic image.

Monoplane analysis: we also attempted to estimate the depth of the catheter tip from the width of the tip electrode seen on a single fluoroscopic image by developing different image processing techniques: manual and automatic binary thresholding, and projection of the greyscale image along a line perpendicular to the axis of the electrode. The projection was carried out after morphological filtering to eliminate the background and rotation of the cropped image through a specified range to find the minimum width of the electrode. Another experiment was performed by incrementally displacing a catheter at known distances away from a fluoroscopic source, in the air. As expected, this analysis showed that the catheter width became smaller as we moved the catheter away from the source. Both binary thresholding algorithms gave an almost perfect correlation for this experimental setup. However, when applied to images obtained from the canine experiment, these algorithms produced unconvincing results. The projection algorithm gave better results: the correlation coefficient between the inverse of the electrode width and the electrode depth was $r = 0.55$ and the standard error of estimate of the electrode depth from the inverse of the electrode width was 58 pixels for the posterior images, whereas we observed $r = 0.66$ and a standard error of estimate of 39 pixels for the left lateral images. These correlation coefficients were statistically significant ($p<0.05$). The standard error of the depth was about 1.5 cm for the posterior views and 1 cm for the left lateral views. The left lateral images always gave better results than the posterior images because of a better contrast

In conclusion, an innovative approach for the fusion of isochronal maps with fluoroscopic images that uses standard catheters and instrumentation was developed. When 3D data was obtained from two projections, appropriate maps that well represented the progression of the electrical activation were generated. When 3D data was obtained from a single image, the standard error of the electrode depth estimate was too large for a precise reconstruction of the cardiac chambers. Better image processing techniques remain to be developed to extract 3D information from a single fluoroscopic image.

CONDENSÉ

Introduction

Certains troubles du rythme cardiaque peuvent être traités par l'ablation par cathéter radiofréquence (RF). La partie du cœur qui dérègle le rythme cardiaque est détruite par un courant RF injecté par un cathéter au voisinage du site arythmogène. Cette procédure est guidée par des images radiographiques obtenues avec un système fluoroscopique. Les taux de succès peuvent atteindre de 90 à 100% pour certaines pathologies comme le syndrome de Wolff-Parkinson-White. Cependant, la précision de la localisation du site arythmogène et le positionnement précis du cathéter RF au-dessus de ce site sont problématiques. Un mauvais positionnement réduit l'efficacité de la procédure et prolonge la durée de l'intervention (typiquement plusieurs heures). Le but de notre travail consiste à développer un nouvel outil de navigation pour raccourcir la durée de la procédure d'ablation et augmenter son efficacité.

Trois systèmes commerciaux qui fournissent une image tridimensionnelle de la séquence d'activation électrique cardiaque ont été proposés récemment pour guider les procédures d'ablations RF. Dans notre travail, nous examinons les avantages et les inconvénients de ces systèmes de cartographie : un cathéter constitué d'un panier déployable comportant 64 électrodes (*Constellation*, EPT Inc.), un cathéter en forme de ballon permettant de calculer les potentiels endocardiques (*Ensite 3000*, Endocardial Solutions Inc.), et un système utilisant des détecteurs magnétiques de position positionnés au bout des cathéters (*CARTO™*, Biosense Webster Inc.) En résumé, les deux premiers systèmes peuvent afficher une carte décrivant la séquence d'activation cardiaque en utilisant des données enregistrées pendant un seul battement tandis que le dernier système utilise des données enregistrées point par point, ce qui implique que l'arythmie doit rester uniforme durant toute la procédure. Tous ces systèmes sont coûteux.

Récemment, notre groupe a tenté de développer un système de navigation fluoroscopique plus abordable qui utilise des cathéters RF standards et un système de fluoroscopie

standard. Le principe de base est de mesurer la position du cathéter sur les images fluoroscopiques ainsi que le temps d'activation locale à cette position, le cathéter est ensuite déplacé à plusieurs autres sites dans le cœur et l'ensemble des données géométriques et électriques est utilisé pour calculer une carte en couleur de la séquence d'activation électrique cardiaque qui est finalement superposée en transparence au-dessus d'une image fluoroscopique du cœur. L'objectif de notre travail a été de poursuivre le développement de ce système de cartographie en effectuant un traitement tridimensionnel des données (plutôt qu'un traitement bidimensionnel) et en développant de nouveaux algorithmes pour estimer la profondeur du cathéter à partir d'une seule image (plutôt que deux images).

Méthodes : l'approche biplanaire

Une expérience fut réalisée sur un chien anesthésié, posé sur une table de fluoroscopie (*Integris Allura*, Philips Inc.) Un cathéter de référence et un cathéter de stimulation furent insérés dans le ventricule droit, proche du septum. Le rôle du cathéter de référence était de définir une origine pour notre système de coordonnées. Ce cathéter de référence a permis de corriger les déplacements du coeur causés par la respiration, le déplacement de l'animal ou le déplacement du système de fluoroscopie. Le rôle du cathéter de stimulation était de produire une séquence d'activation électrique simple pour valider les cartes isochrones. Finalement, un cathéter d'ablation RF ayant un diamètre de 2 mm (taille *7-French*) fut inséré dans la veine fémorale et introduit dans le ventricule gauche. Au cours de l'expérience, ce cathéter de cartographie fut déplacé à 20 sites différents sur la surface interne du ventricule gauche (endocarde) afin d'obtenir les données électriques et géométriques nécessaires pour reconstruire la carte de la séquence d'activation. Des électrogrammes bipolaires furent enregistrés avec le cathéter de cartographie et le cathéter de référence en utilisant un convertisseur numérique/analogique multi-canaux (*PCI DAS-1001*, Omega Inc.). Les électrogrammes furent sauvegardés dans un fichier texte et lus avec le logiciel Matlab 6.1. Le temps d'activation locale fut mesuré (en millisecondes) comme étant la différence de temps entre les déflexions négatives les plus

rapides détectées sur les deux électrogrammes enregistrés avec le cathéter de référence et le cathéter de cartographie.

Le taux d'acquisition des images fluoroscopiques fut réglé à 60 images/seconde afin de minimiser les artéfacts de mouvement. Les images furent enregistrées pendant environ 2 secondes à la fin de l'expiration. Le fluoroscope monoplan fut tourné de 90° pour acquérir deux images pour chaque site: une vue latérale gauche (le fluoroscope est placé verticalement) et une vue postérieure (le fluoroscope est placé horizontalement). Les images furent enregistrées avec une résolution de 512×512 pixels en format *Dicom*. L'image diastolique fut automatiquement sélectionnée pour chaque site afin de mesurer la position des cathéters au même moment durant le cycle cardiaque et ainsi corriger les effets de contraction du cœur. Ceci fut réalisé en identifiant l'image ayant le plus petit écart-type de toutes les différences calculées entre les pixels de l'image et ceux de l'image précédente. Un système de coordonnées fut centré sur l'extrémité du cathéter de référence.

Le logiciel *MatLab 6.1* (*Image Processing Toolbox*) fut utilisé pour le traitement des images. Un algorithme interactif fut développé pour mesurer la position des électrodes au bout du cathéter de référence et du cathéter de cartographie. Premièrement, les images furent manuellement recadrées autour du bout des cathéters. Ces images en teintes de gris furent converties en images binaires (noir et blanc) en utilisant la méthode de Otsu (seuillage automatique). Le centroïde de l'électrode fut alors calculée afin d'obtenir les coordonnées en *XY* et *XZ* pour la vue postérieure et la vue latérale gauche, respectivement. On suppose que le modèle de projection est orthographique, ce qui est une approximation. Nous avons enregistré ces centroïdes afin de reconstruire un modèle en 3D du ventricule gauche.

Méthodes : l'algorithme du polyèdre convexe (convex hull)

L'algorithme du polyèdre convexe (*convex hull*) est une méthode classique et populaire pour construire un objet 3D à partir d'un nuage de points désorganisés. Soit un nuage de points dans un espace en trois dimensions, le polyèdre convexe de ce nuage de points est

un polyèdre dont la surface est constituée de tous les triangles dont les sommets font partie de l'ensemble de points et dont le plan défini par les sommets du triangle sépare l'espace en deux régions : une qui ne contient aucun point et l'autre qui contient le reste des points. Après avoir créé le polyèdre convexe, les temps d'activation mesurés à chaque sommet furent linéairement interpolés sur la surface de chaque triangle du polyèdre et affichés en couleur, en utilisant le rouge pour l'activation la plus précoce et le bleu pour l'activation la plus tardive. Afin de tracer seulement les triangles qui peuvent être vus d'un certain point de vue, la normale à la surface de chaque triangle du polyèdre fut calculée (les normales pointent vers l'extérieur du polyèdre), et si leur produit scalaire avec le vecteur du point d'observation était positif, le triangle était retenu pour reconstruire la carte isochrone en 2D. Par exemple, pour la vue postérieure nous avons tracé tous les noeuds associés avec un triangle dont la composante normale était positive selon la direction Z.

Méthodes : l'approche monoplanaire

Les systèmes de fluoroscopie biplanaires sont rares à cause de leur prix élevé (environ le double d'un système monoplanaire). Par ailleurs, obtenir deux projections en tournant un fluoroscope monoplanaire à chaque site visité par le cathéter prend beaucoup de temps. Ainsi, il y a un besoin évident pour calculer la profondeur du cathéter à partir d'une seule image. En effet, la profondeur de l'électrode peut être théoriquement obtenue à partir de sa largeur puisque la projection d'un objet devient plus grande lorsque celui-ci s'approche de la source de rayonnement. Deux approches de traitement d'images furent développées pour déterminer la largeur en pixel de l'électrode: le seuillage et la projection après filtrage. Pour ces deux approches, les images postérieures et latérales gauche furent complémentées et le contraste fut amélioré en étirant l'histogramme des intensités.

Pour la première approche, l'image fluoroscopique de l'électrode (recadrée dans une petite fenêtre) fut convertie d'une image en teintes de gris à une image binaire en utilisant l'algorithme de seuillage manuel et un algorithme de seuillage automatique développé par Otsu. Ensuite, nous avons manuellement sélectionné l'électrode parmi les objets

présents dans la petite fenêtre. La longueur de l'axe mineur de l'ellipse ayant le même second moment que l'électrode fut calculée afin d'estimer la largeur de l'électrode. Cette valeur est forcément approximative puisque la projection de l'électrode n'a pas exactement la forme d'une ellipse

La deuxième méthode fut basée sur la projection de l'image en teintes de gris le long d'une ligne perpendiculaire à l'axe de l'électrode. Mais tout d'abord, un filtrage morphologique fut appliqué à l'image recadrée afin d'éliminer les éléments de fond autour de l'électrode. Nous avons soustrait de l'image originale, l'image morphologiquement filtrée par une opération d'érosion suivie par une opération de dilatation utilisant une balle, un disque et un diamant comme élément structurant (c'est-à-dire une matrice de 0 et 1 dont le pixel du centre de l'élément structurant identifie le pixel d'intérêt). Deuxièmement, l'image fut tournée de façon à ce que l'axe de l'électrode soit vertical. Ensuite, les valeurs de chaque pixel d'une colonne donnée furent additionnées, et ceci fut répété pour chaque colonne. Cette projection produit une courbe en forme de cloche. Finalement, un seuil fut fixé à 50% du maximum de cette courbe, sur les pentes, pour une analyse plus robuste. Les deux points d'intersection de la courbe avec le seuil furent calculés par interpolation linéaire pour estimer la largeur de l'électrode. Pour bien s'assurer que la projection de l'électrode soit la plus petite possible, l'image de l'électrode fut tournée dans une plage de $\pm 20^0$ autour de la position verticale et la plus petite valeur de la largeur fut retenue.

Résultats

En utilisant l'approche bi-planaire, la superposition de la carte isochrone en 2D (la projection du polyèdre convexe à partir d'un point de vue) au-dessus de l'image fluoroscopique correspondante a été réalisée sur les deux vues postérieure et latérale gauche. Le rapport de transparence fut fixé à 30% pour la carte isochrone et 70% pour l'image fluoroscopique. Ces pourcentages nous permettent de bien visualiser les contours du cœur dans l'image et la carte isochrone de la séquence électrique en couleur. Le cathéter de référence fut identifié sur l'image fluoroscopique par un « X ». Les temps

d'activation les plus précoces étaient visiblement plus près du cathéter de stimulation. L'image de la vue postérieure montrait une carte isochrone dont le contour suivait la forme du cathéter de cartographie, qui correspondait aussi au contour de la cavité ventriculaire gauche.

Pour évaluer l'exactitude de l'approche monoplanaire, nous avons d'abord réalisé une expérience simple où le cathéter était déplacé dans l'air, à des distances connues de la source de rayonnement (en millimètres), le long de l'axe entre la source et le centre de l'amplificateur de brillance du fluoroscope. Nous avons calculé le coefficient de corrélation (r) entre l'inverse de la largeur projetée de l'électrode (en pixel) et la profondeur de cette même électrode. En utilisant l'algorithme de seuillage manuel (niveau=0.16), nous avons obtenu r=0.9988 et une erreur-type de prédiction de la profondeur à partir le la largeur de 3.6 mm; pour l'algorithme de seuillage automatique, nous avons obtenu r= 0.998 et une erreur-type de 4.7 mm.

Par contre, pour les images obtenues chez l'animal et pour lesquelles la profondeur du cathéter était mesurée sur l'image perpendiculaire (en pixels), la méthode de seuillage s'est avérée inefficace: pour le seuillage manuel (niveau=0.16) appliqué aux images postérieures, aucun résultat concluant ne fut obtenu car certaines estimations de la largeur étaient irréalistes, tandis que pour la vue latérale gauche, le coefficient de corrélation était de r=0.38. Les résultats furent légèrement meilleurs pour le seuillage automatique : les coefficients de corrélation étaient r=0.17 pour la vue postérieure (statistiquement non significative) et r=0.51 pour la vue latérale gauche ($p<0.05$). L'erreur type d'estimation pour la profondeur était de 69 pixels pour l'analyse de la vue postérieure et de 44 pixels pour l'analyse de l'image latérale gauche. Les résultats obtenus avec l'approche de projection après filtrage furent plus favorables, les coefficients de corrélation étaient statistiquement significatifs ($p<0.05$) avec r= 0.55 pour la vue postérieure et r= 0.66 pour la vue latérale gauche. L'erreur type d'estimation de la profondeur calculée à partir de l'inverse de la largeur était de 58 pixels pour la vue postérieure et de 39 pixels pour la vue latérale gauche. Pour interpréter ces erreurs en termes de millimètres, rappelons que pour la vue postérieure, la largeur de la projection de l'électrode s'étendait entre 7.4 et 9.6

pixels avec une valeur moyenne de 8.5 pixels, tandis que pour la vue latérale gauche, la largeur variait entre 7.1 et 8.9 pixels avec une valeur moyenne de 8 pixels; puisque le diamètre du cathéter était de 2 millimètres, ceci indique que l'erreur type d'estimation de la profondeur était environ 15 mm pour la vue postérieure et 10 mm pour la vue latérale gauche.

Discussion

Dans le cas de l'approche biplanaire, les sites visités par le cathéter dans le ventricule gauche ont pu être représentés par un polyèdre convexe et les cartes isochrones en 2D ont pu être superposées sur les images fluoroscopiques correspondantes. Ces cartes ont bien décrit la progression de l'activation loin du cathéter de stimulation. L'acquisition de données a pris approximativement 30-40 minutes. À cause du mode d'enregistrement point-par-point, nous pouvons seulement analyser des arythmies soutenues et uniformes avec cette approche.

De plus, les mesures séquentielles des images fluoroscopiques horizontales et verticales n'étaient pas aussi précises que des mesures simultanées avec un véritable fluoroscope biplanaire car la position verticale du cathéter de référence a montré une petite différence de 4±17 pixels entre les images postérieures et les images latérales. On peut expliquer cette petite différence par des artéfacts de mouvement (respiration, battement de coeur, déplacement du sujet) et la possibilité que le fluoroscope ne soit pas bien aligné. En terminant, les images n'ont pas été calibrées car il n'y a pas besoin de transformer les valeurs en pixel des coordonnées d'image, en valeurs en millimètre d'un système de coordonnées universel étant donné que les cartes isochrones 2D sont toujours tracées dans les coordonnées d'image pour la superposition avec les données fluoroscopique.

Dans le cas de l'approche monoplanaire, bien que la méthode de projection après filtrage morphologique ait produit de meilleures estimations de profondeur que la méthode de seuillage automatique, les résultats furent décevants puisque l'erreur type de l'estimation de la profondeur était trop grande pour la construction précise d'un polyèdre convexe. Le contraste de l'image fluoroscopique affecte l'exactitude des évaluations de profondeur:

une analyse visuelle a indiqué que les images latérales avaient toujours un meilleur contraste que les images postérieures en raison de la section oblongue du torse canin et ces images latérales ont systématiquement fourni de meilleures évaluations de profondeur.

Conclusion

Une approche innovatrice pour la fusion des cartes isochrones avec des images fluoroscopique et employant une instrumentation standard a été mise en application. Les résultats furent satisfaisants lorsque les données 3D furent obtenues par une approche biplanaire, mais non satisfaisants lorsque la profondeur des cathéters fut estimée avec l'approche monoplanaire. De meilleures techniques de traitement d'image restent maintenant à être développées afin d'extraire l'information 3D appropriée à partir des images 2D fluoroscopiques pour l'approche monoplanaire. Par exemple, on pourrait tenir compte de la dynamique cardiaque d'où une approche de reconstruction 3D est analysée à partir d'une séquence monoplan.

TABLE OF CONTENTS

LIST OF TABLES

LIST OF FIGURES

Chapter 1

Introduction and Objectives

1.1 Mapping out the Problem

Sudden Cardiac Death (SCD) is the number one cause of death in the United States and Canada, accounting for more than 400,000 and 45,000 deaths each year in these two countries, respectively [1]. The mechanism of SCD involves fast cardiac rhythms called tachyarrhythmias: a normal heart rate ranges between 60 and 100 beats per minute whereas a person affected by tachyarrhythmias can have heart rhythms greater than 100 beats per minute. Some tachyarrhythmias can be of minimal consequence to some people, but can also lead to cardiac arrest if not treated.

Today, advanced technology and medication have helped treat many health disorders and prolong the quality of life in people. Tachyarrhythmias can be treated in several ways. In the simplest case, patients can be given doses of antiarrhythmic drugs that will help slow down the electrical conduction in the heart. In other cases, an internal or an external defibrillator will deliver an electric shock to the heart with the aim of reestablishing regular rhythm. An alternative method is called radio-frequency ablation. Here, a catheter is guided in the heart's chamber affected by the arrhythmia, and burns off a small region of the heart that causes the tachyarrhythmia by injecting radiofrequency currents (500 kHz, 10-20 watts) through the tip electrode of the catheter.

The radio-frequency ablation treatment requires the use of a fluoroscope (Figure 1.1). This implies obtaining an X-ray image from a patient. The X-rays pass through the patient and strike a fluorescent plate that is scanned by a television camera. The cardiologist can observe what is happening on the screen [2]. The problem lies with the amount of radiation exposure. By minimizing radiation exposure, we in turn diminish the

risk of skin injury. In one study, it was estimated that each hour of radiation exposure was associated with an increase in lifetime risk of fatal cancer of 0.1 percent [3].

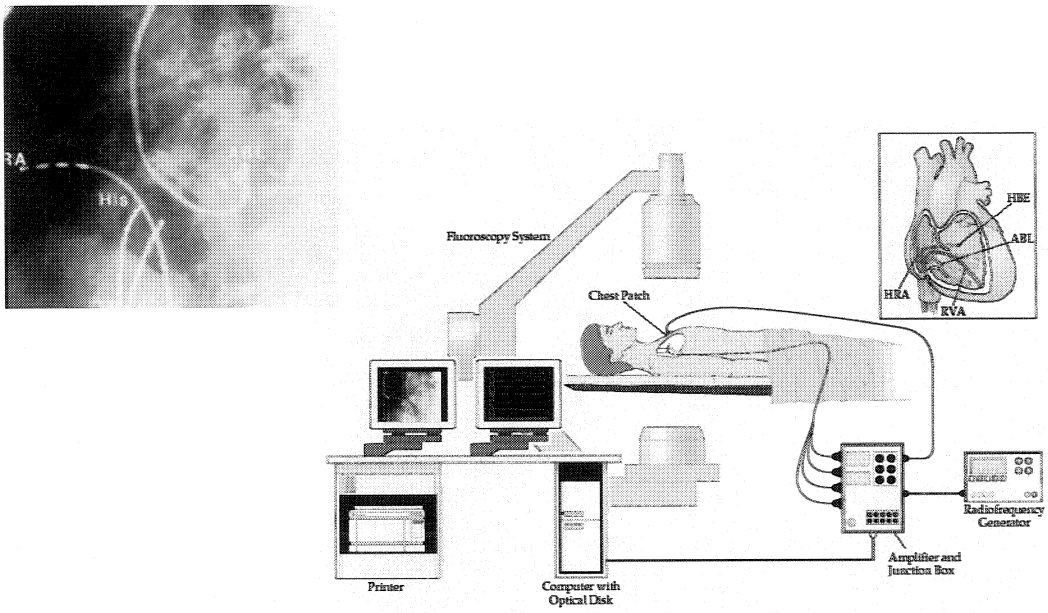

Figure 1.1 Fluoroscopic Imaging in RF Ablation Procedures [4].

Another difficulty lies with the total duration of the RF ablation procedure. In some cases, the ablation intervention varies anywhere from 1 to 10 hours. The problem is actually finding the site of origin within the heart where excess firing of cells occur. To reduce substantially the ablation duration, newer technology has made it possible to draw the heart as a 3D model for the cardiologist to examine. Not only is the heart displayed in 3D, the actual sequence of the electrical activation is color coded as well. This activation sequence displays the site of origin of the arrhythmia.

1.2 The Proposed Approach

If we can somehow limit the expenses by actually developing a novel approach in treating arrhythmias, then we could envision the reduction in costs, and the increase of ablation procedures on a yearly basis. How many hospitals can afford to purchase a single mapping system worth approximately 400,000$? And how many mapping systems are needed to meet the demands of an aging population of patients that is more likely to experience severe arrhythmias?

Preliminary work has been done at Sacré-Coeur Hospital to develop an affordable fluoroscopic navigation system by Sierra et al. [1], who introduced the concept of "fusion mapping". Fusion mapping consists of superposing an isochronal map depicting the electrical activation sequence over a fluoroscopic image of the cardiac region (Figure 1.2). The isochronal maps are obtained by moving the RF catheter at multiple sites inside the heart chamber and by measuring the local electrical activation time at each site. The successive positions of the catheter are measured from the fluoroscopic images and combined with the corresponding activation time to plot the isochronal map. This cost effective alternative is user friendly for cardiologists who already use fluoroscopy to guide RF ablation on a routine basis.

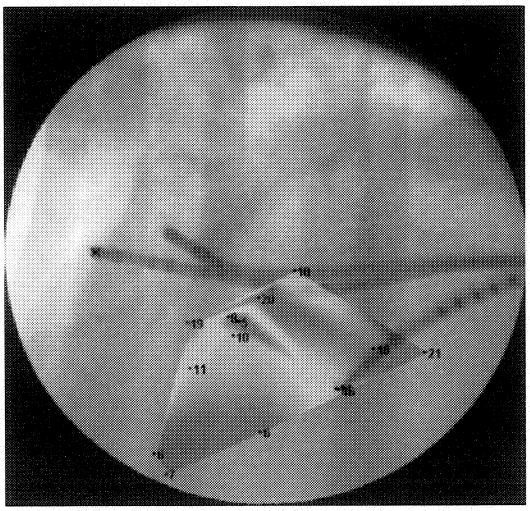

Figure 1.2 Superposition of an isochronal map depicting the cardiac electrical activation sequence over the corresponding fluoroscopic image of the canine heart that encloses ablation catheters. The numbers indicate local activation time (ms) at each catheter site and the color progression (from red to blue) indicates the earliest to the latest local activation times. The mapping catheter was successively moved at about 20 sites [1].

The preliminary results of Sierra et al. [1] need much improvement to come close to emulating the mapping systems that are already available on the market. The following questions must be addressed:

- How to obtain 3D geometrical data about catheter locations from 2D images?
- How to describe the geometry of the surface that encloses all the 3D electrode locations inside the cardiac chamber so that it can be visible from a specific vantage point?
- How to correct for motion artifacts due to the beating of the heart as well as the patient's respiration?
- Finally, is the proposed technique feasible in a clinical context?

1.3 Outlook of Chapters

Chapter 2 begins by illustrating the physiological aspects of the heart and the different types of tachyarrhythmias that can be treated by catheter ablation. We will present the different mapping systems that are currently on the market and that aid in guiding catheter ablation. We will compare the effectiveness of each one and discuss the expectations of our proposed system. Finally, we will review the algorithms that could be used to answer our first question on the construction of a surface that encloses our measurement points.

The structure of the next two chapters is non-standard since each chapter includes both a description of methods and the corresponding results. We hope that this structure will be clearer for the reader.

Chapter 3 will specifically address the question of obtaining 3D geometrical data from 2D images by using fluoroscopic data from two perpendicular images of the catheter at the same site and is thus entitled: "biplane analysis". The questions of describing the surface that encloses the measurement points and of correcting for motion artifacts will

also be addressed with different methodologies. Finally, fusion maps obtained during an animal experiment will be presented.

Chapter 4 will address the question of obtaining 3D data from 2D images by using a single image of the catheter and is entitled: "monoplane analysis". We describe the different methods that we developed to compute the depth of the catheter from the apparent size of the electrodes. Results are presented for different experimental setups: the catheter is moved at known intervals in the air, the catheter is moved at different locations inside the cardiac chamber.

Chapter 5 discusses the results and presents conclusions and suggestions for ulterior work.

Chapter 2

Review Of Literature: Physiology, Mapping Systems and Reconstruction Algorithms

2.1 Cardiac Physiology

The heart is made up of four chambers – two upper atria and two lower ventricles – separated by a wall and valves. When a chamber is relaxed, or expanded, it is in *diastole*. Whereas a chamber that is in contraction is said to be in *systole*. The heart's electrical rhythms begin as impulses emitted from the sinus node (S-A node), the heart's "natural pacemaker" (Figure 2.1). The S-A node is a small cluster of specialized cells located in the right atrium, the upper right chamber of the heart. At the onset of the heart cycle, impulses from the SA node induce the right atrium to depolarize. This depolarization spreads across the atrial muscle causing atrial contraction, increasing atrial pressure and forcing blood into the ventricles. The ventricular contraction phase of the heart cycle is brought about by depolarisation of the ventricles via the atrioventricular (AV) node,

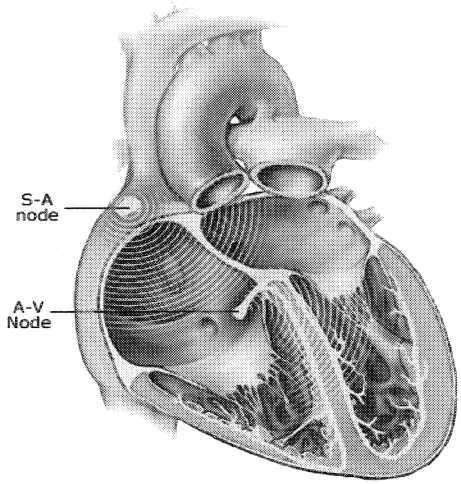

Figure 2.1 Electrical pathways in heart [7].

Bundle of His and the Purkinje fibers. The AV node provides a delay time allowing the atria to pump blood into the ventricles before ventricular contraction. The Bundle of His and Purkinje fibers allow the ventricles to be depolarized rapidly [8].

Figure 2.2 illustrates the normal electrocardiogram (ECG), which is a recording of low-level potentials (mV) on the surface of the torso. The ECG is composed of a P wave, a QRS complex and a T wave. The P wave reflects the depolarization of both atria, whereas the QRS complex and T wave reflects the depolarization and repolarization of the ventricles, respectively [8].

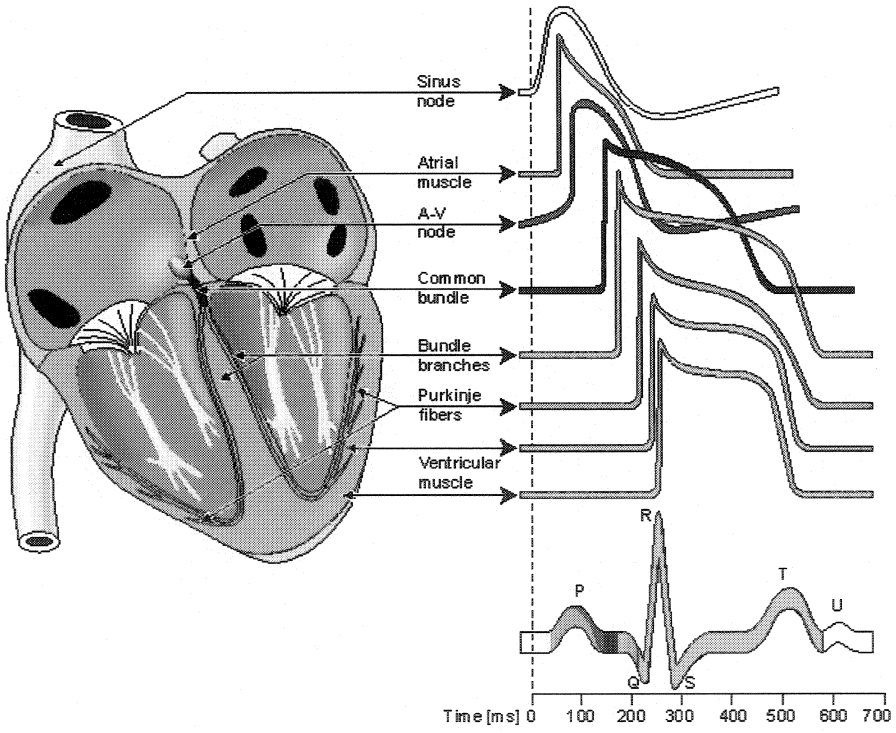

Figure 2.2 The ECG composed of the P wave, QRS complex and T wave [8].

2.2 Activation Time Measurements

Cardiac electrical activation is determined by action potentials propagating between cells. This phenomenon is explained by the depolarization of cells either spontaneously or assisted by external stimulation. Let us consider a cell at rest with a resting membrane potential of 85 mV. By injecting positive charges near the cell and hence making the membrane increasingly positive, an action potential is created. Electric charges then travel to neighboring cells through inter-cellular junctions and triggers new action potentials. This cascade effect leads to the propagation of the electrical activation within the heart [18]. Figure 2.3 represents a diagram of a block of ventricular myocardium. An electric stimulus is applied to the left, which triggers an action potential that propagates from left to right. At each time instant, the traveling activation front can be represented by an equivalent current dipole that moves from left to right (horizontal arrows). For an electrode placed at point A, the potential is always negative because the electrode is behind the dipole throughout the propagation and the amplitude decreases as the dipole travels further away from it. For an electrode stationed at point B, the potential becomes ever more positive as the dipole nears, and then becomes negative as the dipole passes it and continues further to the right. Finally at point C, the potential becomes more positive and then returns to zero once the activation front ceases to exist. In every case, the electrogram will always show a rapid negative deflection once the activation front passes

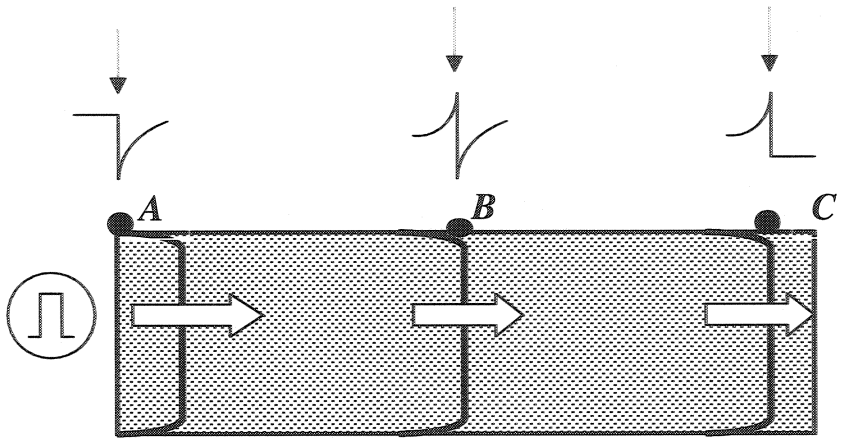

Figure 2.3 Depolarization sequence due to external stimuli from electrode [18].

right under the electrode. The vertical arrows pointing down on each of the three small potential diagrams demonstrate this. By measuring the time at which this deflection occurs in every electrogram recorded in the heart, we are able to construct an isochronal map illustrating the electrical activation sequence.

2.3 Tachyarrhythmias

2.3.1 Ventricular Tachycardia

A rather severe form of tachyarrhythmia occurs when the heart's electrical signals originate from one of the ventricles, instead of the correct location in the S-A node (Figure 2.4). This causes a type of arrhythmia called ventricular tachycardia (VT) with very fast heartbeats typically between 150 to 200 beats/min.

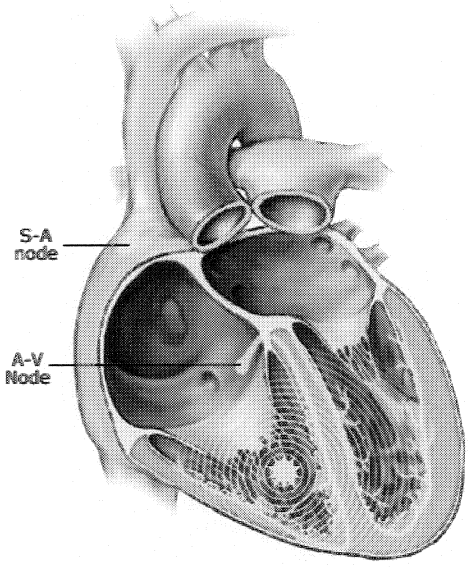

Figure 2.4 Ventricular Tachycardia [9].

leaves insufficient time for the heart to fill between beats. If this rampant heartbeat persists, the brain may not receive an adequate supply of blood and oxygen, thus provoking possible fainting spells, blackouts, temporary blind spots or dizziness [9].

2.3.2 Atrial Tachycardia

Atrial tachycardia refers to a rapid heart rate caused by stimuli from within the atria. The rate of atrial impulses can range from 300-600 beats/min. This very rapid rate greatly increases the heart's workload while decreasing the amount of time the heart has to fill with blood, thereby reducing heart function [10].

2.3.3 Re-Entrant Tachycardia

The key feature of re-entrant arrhythmias is that the wave front re-enters previously excited tissue to depolarize it again (Figure 2.5). If the re-entrant activity is maintained and has a rapid enough rate, it produces a sustained tachycardia. Heart rate may be in the range of 130 and 250 beats/min [12].

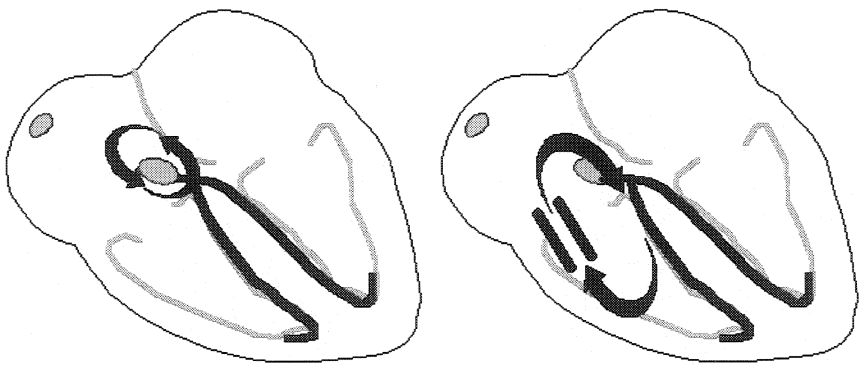

Figure 2.5 (Left): Nodal reentrant tachycardia. (Right): AV reentrant tachycardia [12].

2.4 Radiofrequency (RF) Ablation

Since its initial successful application, RF ablation has become the most common technique for treating cardiac arrhythmias along with medication therapy. RF ablation is a technique whereby a physician inserts a catheter through a blood vessel (usually in the upper thigh) and directs it into a specific location within the heart. At the tip of the tube is a small electrode, which can deliver radiofrequency energy to burn away the abnormal tissues of the heart that are the root cause of arrhythmia [11].

The entire procedure generally involves placing three to five catheters into the heart via the femoral or internal jugular veins (Figure 2.6) under fluoroscopic guidance. The catheters are positioned in specific points in the heart to stimulate the heart and to record local activation times to help locate the abnormal tissue that is causing the arrhythmia and that is usually associated with the earliest local activation time [11].

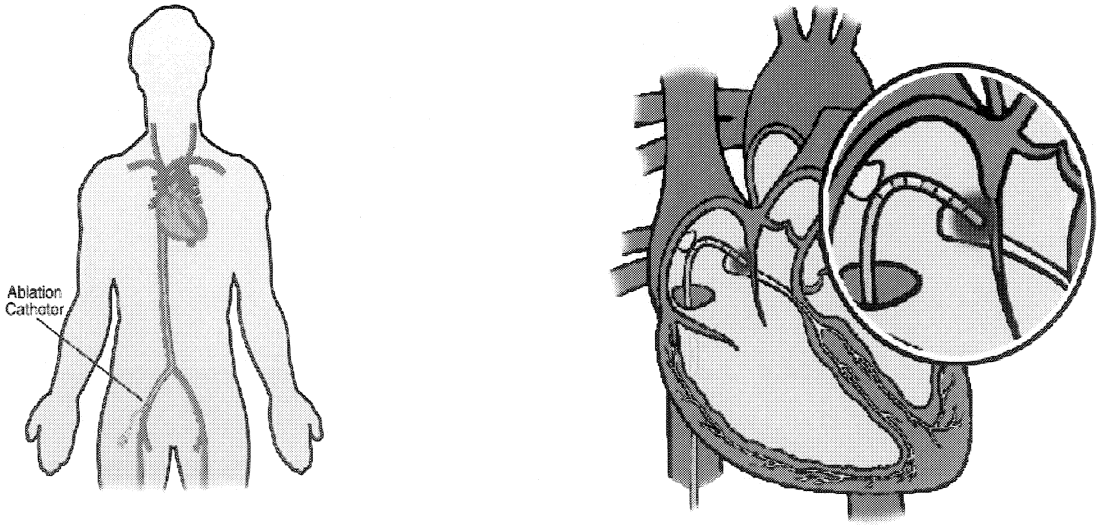

Figure 2.6 Ablation Catheter Insertion [4].

However, this approach is considered problematic for a number of reasons, such as [14]:

- The endocardial surface is invisible using fluoroscopy and the target sites can only be approximated by their relationship with nearby structures such as ribs, blood vessels, and the position of catheters.
- Due to the limitations of two-dimensional fluoroscopy, navigation is imprecise, time consuming, and requires multiple views to estimate the three-dimensional location of the catheter.
- Exposure of the patient and medical team to radiation.
- The inability to accurately associate intracardiac electrograms with their precise location within the heart [14].

In order to improve the effectiveness and safety of catheter ablation, new technical developments have been introduced lately. Using workstations, these systems generate three-dimensional color-coded isochronal maps that guide catheter ablation. We will now present these systems and compare their advantages and disadvantages.

2.5 Commercial 3D Mapping Systems

2.5.1 Contact Mapping System: CARTO XP

The CARTO XP ablation mapping and navigation system provides real-time data on three-dimensional, color-coded maps of the electrical activity of the heart. The CARTO XP system makes possible precise, real-time tracking of catheter location by using magnetic fields.

The mapping catheter resembles a standard deflectable ablation catheter with a 4-mm tip and proximal 2-mm ring electrodes. The location sensors lie adjacent to the tip electrode, totally embedded within the catheter. The three location sensors are located orthogonally to each other. A locator pad is placed beneath the operating table and includes three coils

that generate low magnetic fields, which decay as a function of the distance from their sources (Figure 2.7).

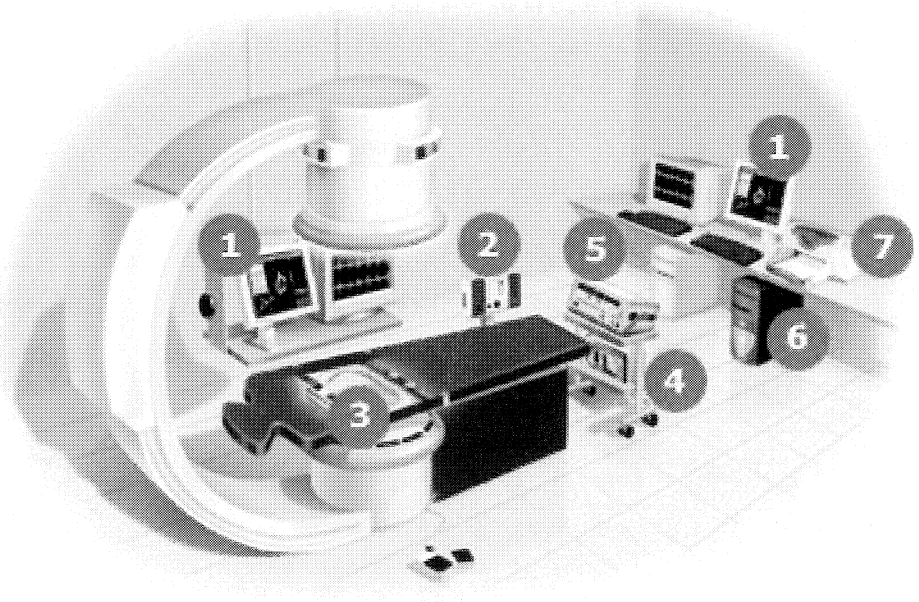

Figure 2.7 1. Flat screen monitors; 2. Patient Interface Unit; 3. Location Pad; 4. CARTO XP COM Unit, 5. Stockert RF Generator; 6. PC workstation; 7. Color printer [15].

When the catheter is moved within this magnetic field, signals received by the sensors are transmitted along the catheter shaft to the main processing unit so as to track its position in three dimensions. The spatial resolution of the system has been previously shown to be <1 mm in both in vitro and in vivo studies. This approach enables tracking of the catheter independent of fluoroscopy.

In practice, a first catheter is introduced inside the coronary sinus or in the right ventricle so as to serve as an anatomical reference, and a second mapping catheter is introduced in the cardiac chamber to be investigated. The mapping system determines the location and orientation of both the mapping and reference catheters at a specific time instant during the cardiac cycle. The location of the mapping catheter is measured relative to the

location of the reference catheter, thus compensating for motion artifacts (cardiac, respiratory and subject motion). By moving the catheter inside the heart, the system continuously analyzes its location, it also measures the local activation time from the electrogram recorded at that location and using the data from multiple points, generates a 3D isochronal map [13].

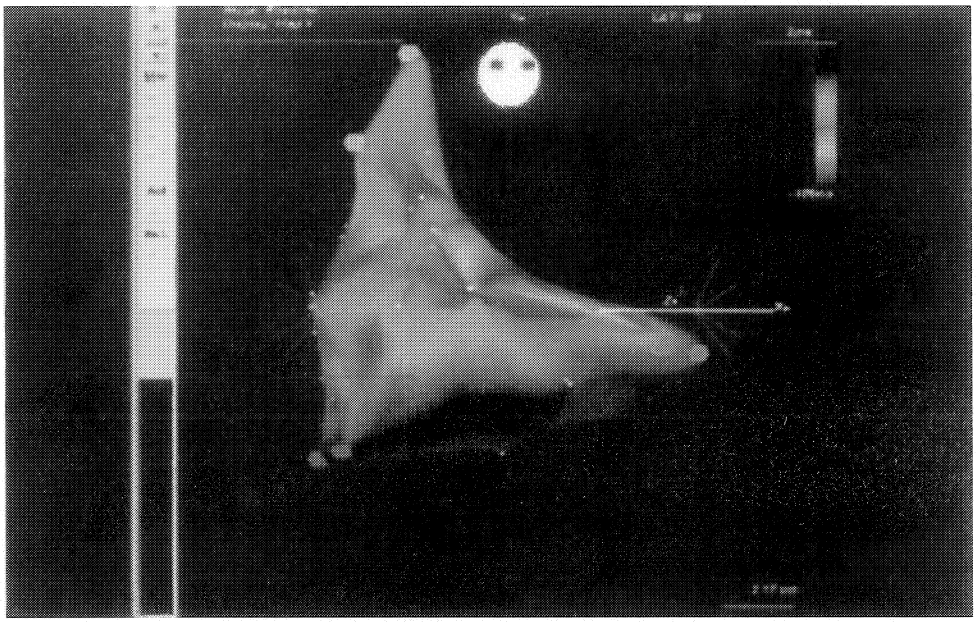

Figure 2.8 3D isochronal map generated by the CARTO system [13].

2.5.2 Non-Contact Endocardial Mapping: EnSite 3000

The EnSite 3000 system provides electrophysiologists with a real time, virtual image of the electrical activity of the heart without contacting the heart's surface. The electrode array consists of a small balloon around which are woven 64 insulated wires with a single break in their insulation, producing 64 unipolar electrodes (Figure 2.9). This array is mounted at the end of a catheter, which is introduced in the cardiac chamber to be investigated. When placed in the chamber, the small balloon is partially inflated. The

balloon does not fill the chamber and the electrodes do not make contact with the cardiac wall (which is why this approach is called "non-contact"). A multi-channel amplifier and computer workstation processes the raw far-field electrographic data.

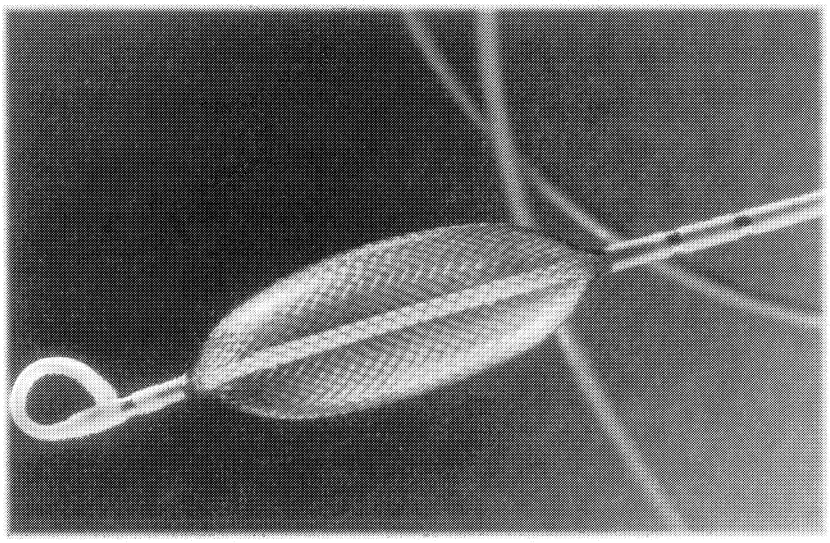

Figure 2.9 EnSite 3000 catheter balloon [13].

The system is used in three steps:

1. The cardiac chamber geometry is established.
2. Site(s) critical for maintenance of re-entry circuit(s) are identified from maps.
3. Ablation catheter is navigated to critical site(s) [13].

A catheter "locator" system is used during steps 1 and 3. An electrical signal emitted by the mapping/ablation catheter allows its position to be determined relative to the electrode array. It can be used to construct a three-dimensional computer model of the endocardium (virtual endocardium) by moving the conventional catheter around the cardiac chamber, thus building a series of coordinates for the endocardium. During step 2, endocardial electrograms computed from the 64 measured electrograms using the computer model are then superimposed onto the virtual endocardium to produce

isopotential maps [13]. The computation of the endocardial electrograms is based on the inverse solution of the Laplace equation.

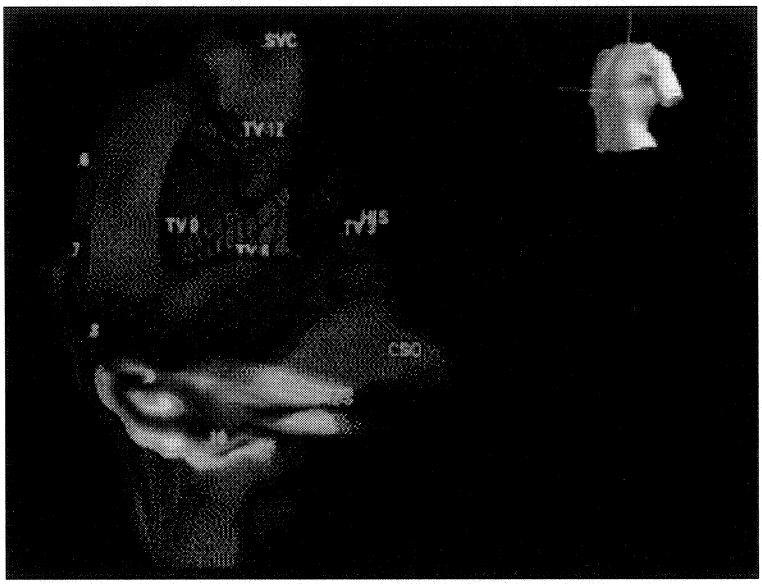

Figure 2.10 3D Mapped volume with electrical isochronal activation map for Ensite 3000 [16].

2.5.3 Basket Catheter: Constellation

Simultaneous mapping of multiple points is performed using a 64 lead basket catheter that can be deployed percutaneously. Current designs of basket arrays consist of a series of equally spaced electrodes mounted on eight flexible splines (Figure 2.11). Each spline contains eight 1.5 mm electrodes with 3-mm spacing. The catheter is introduced percutaneously through a sheath into the chamber. By pulling back the sheath, the splines deploy and are apposed against the endocardium [13].

The basket catheter as illustrated in Figure 2.11 is connected via amplifiers to the mapping system. The signals are filtered from 30 to 400 Hz. Detection of local activation

is performed for each electrogram and two-dimensional isochronal maps are generated [13].

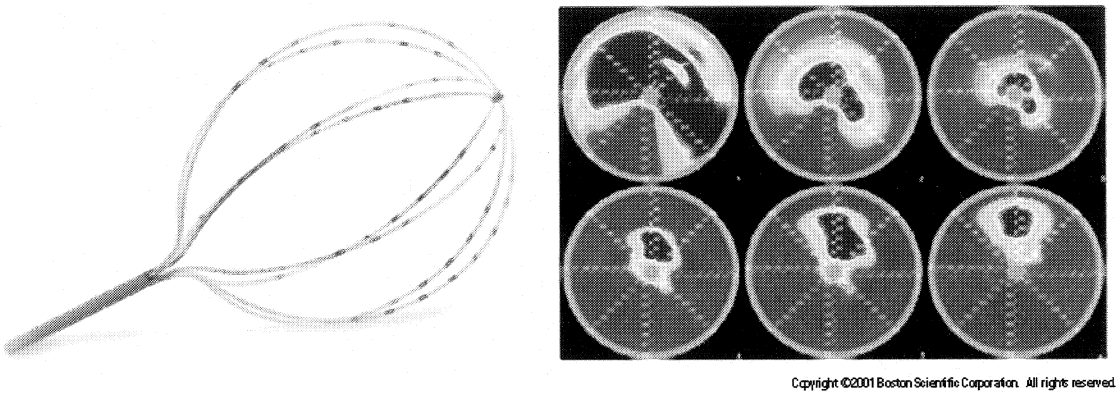

Figure 2.11 Basket Catheter (left) with isochronal maps (right) [17].

2.6 Advantages and Disadvantages of each system

2.6.1 Contact Mapping System: CARTO XP System

Advantages:

- The CARTO technology enables one to perform the mapping procedure and to potentially define the mechanism underlying the arrhythmia, to design an ablation strategy, and finally to navigate back to the desired site for the delivery of RF ablation within 1mm of the focal point.

- It allows the user to associate the intracardiac electrogram with the reconstructed three-dimension anatomy (electroanatomic mapping), which helps to determine the site of arrhythmia origin.

- The catheter can be relocated accurately to the points of interest and it also considerably reduces fluoroscopic exposure to radiation.

- Important cardiac structures such as the His bundle, ostia of venous structures, valve annuli and scar tissue can be tagged properly, which are avoided during ablation. The ability to tag previously unsuccessful ablation sites also helps to identify the correct location for ablation [13].

Disadvantages:

- The CARTO system is limited to point-to-point mapping. Hence, if the arrhythmias are non-sustained or quickly change to a different morphology or mechanism (e.g., atrial tachycardia degenerating to atrial fibrillation), mapping of such arrhythmias will be impossible to complete [13].

2.6.2 Non-Contact Endocardial Mapping: EnSite 3000

Advantages:

- The main advantage of Ensite 3000 is that it requires only one beat to reconstruct a complete activation map, which potentially allows mapping of hemodynamically unstable arrhythmias.

- The system can, from the measured potentials, reconstruct and interpolate about 3300 electrograms simultaneously with high-resolution [13].

Disadvantages:

- The distance between the endocardial wall and the balloon center, as well as the spatial complexity of the activation patterns influences the accuracy of the electrogram reconstruction negatively. This will affect the reliability when mapping dilated left ventricles or complex re-entrant circuits.

- Despite several software updates, the system is still quite complex, expensive, and for large target chambers the accuracy to localize the origin of focal activity decreases considerably.

- Accuracy of reconstruction of endocardial electrograms is dependent on the solution of the Laplace equation, the regularization technique used and the accuracy of the geometry matrix. Errors in geometry will still occur and may be related to the number of endocardial points sampled and the complexity of the geometry of the chamber [13].

2.6.3 Basket Catheter: Constellation

Advantages:

- It provides simultaneous, multiple, stable recordings for most of the endocardial surface. Depending on the location of the arrhythmogenic substrate a complete coverage of the re-entry circuit is possible.

- In addition to multiple simultaneous recordings, the basket catheter provides stable, multiple pacing sites distributed throughout the chamber where it is deployed. Thus, the ablation of arrhythmias could be remarkably facilitated.

- The color-coded animation images simplify the analysis of multielectrode recordings and help in establishing the relationship between activation patterns and anatomic structures [13].

Disadvantages:

- Basket catheters, do not for all points, orient themselves towards the endocardium in the shape expected and this may impair our judgment.

- Basket catheters have a relatively large area near the shaft without electrodes, therefore some part of the endocardium is not in contact with the basket. The quality of recordings is critically dependent on proper selection of basket size.

- There is a potential risk of thrombo-embolism with left sided mapping [13].

2.7 Present Situation of Proposed Mapping Technique

The estimated costs (in Canadian dollars) for each system are as follows:

1. CARTO : ~360,000$ + 5,000$ for each catheter
2. Ensite 3000: ~390,000$ + 5,100$ for each catheter
3. Constellation Basket: ~100,000$ + 5,000$ for each catheter

One of the advantages of our experimental procedures is that we will be using standard ablation catheters that are not expensive (<$1000).

Our research is intended to help develop a novel fluoroscopic navigation system that can treat any complex arrhythmia. This will be achieved by emulating the CARTO procedure using a point-by-point technique. Again, the disadvantage of this procedure is that we need to relocate the mapping catheter inside the ventricle at many points. This is time consuming. However, our electrograms will be accurate and will not rely on interpolation algorithms like those of the Ensite 3000 system.

2.8 Unorganized Point Clouds: 3D Surface Reconstruction Algorithms

Numerous meshing algorithms have been developed for the purpose of reconstructing a surface given an initial set of unorganized three-dimensional points. Most of these are based on triangulation methods that create triangles or tetrahedrons using the unorganized points as vertices. The natural build up of the reconstructed surface happens when these triangulations are joined one after the other. We introduce four classical algorithms that are currently being used in a medical context worldwide. These include: *Delaunay Triangulation & Voronoi diagrams, the Crust algorithm, Growing Cell Structures, and the Convex Hull.*

2.8.1 Delaunay Triangulation

"Meshing" is a popular term in surface reconstruction. It involves the creation of polygons, polyhedrons, triangles, etc., that contain the unorganized three-dimensional points [21].

The Delaunay Triangulation (DT) is one of these meshing methods. The DT of a set of points is defined as a triangulation of that set in which the circumcircle of every triangle does not contain any other points from the set (the circumcircle is the circle that passes through the 3 nodes of the triangle). This property is also referred to as the empty-circle property. The empty-circle property can also be defined for the edges of a mesh: an edge is called legal or Delaunay when the circumcircle of its incident triangles do not contain the opposite node of the other triangle (Figure 2.12). Delaunay triangulation and Delaunay edges are intimately related: a Delaunay triangulation only has Delaunay edges [22].

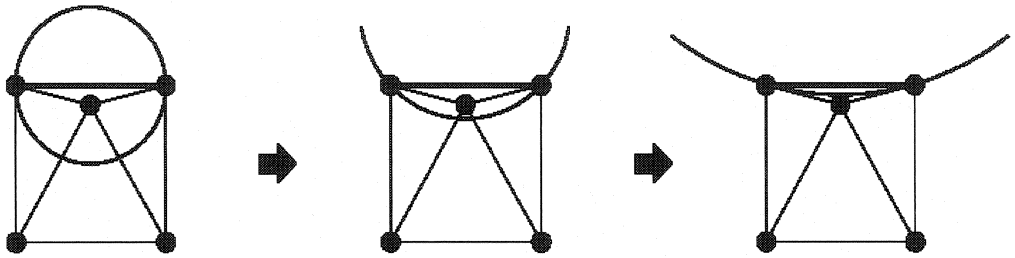

Figure 2.12 An empty circle that passes through two vertices (edge) defines Delaunay triangulation in 2D [23].

If an edge is illegal, then the algorithm will search for another solution. A test for illegality is performed (Figure 2.13). We introduce this concept by stating the following definition:

Definition: Let edge ($p_i\ p_j$) be incident to triangles $p_i\ p_j\ p_k$ and $p_i\ p_j\ p_l$, and let C be the circle through p_i, p_j and p_k. The edge($p_i\ p_j$) is illegal if and only if the point p_l lies in the interior of C. Furthermore, if the points p_i, p_j, p_k, p_l form a convex quadrilateral and do not lie on a common circle, then exactly one of $p_i\ p_j$ or $p_k\ p_l$ is an illegal edge [24].

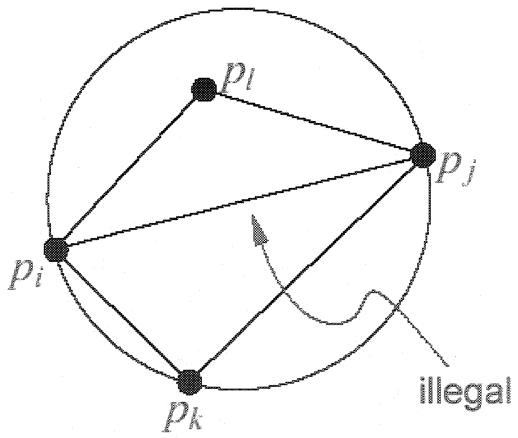

Figure 2.13 Test for illegality of edges in a 2D Delaunay Triangulation [24].

Given: Point set P = $\{p_1 \ldots, p_n\}$
Initially:
Compute triangle (x,y,z),
Which include the points $p_1, \ldots, p_n$.

Algorithm Delaunay Triangulation *DT(P)*

- $m = \max\{ |x_i| |y_i| \}$
- $T = \Delta((3m,0), (-3m,-3m), (0,3m))$

1. initialize *DT(P)* as *T*
2. permutate the points in *P* randomly
3. for $r = 1$ to n do
   find the triangle in *DT(P)*, which contains p_r;
   insert new edges in *DT(P)* to p_r;
   legalize new edges.

4. remove all edges, which are connected with x, y, or z

Inserting a point

Two cases: p_r is inside the triangle, or p_r is on an edge

Legalize (p_r, edge($p_i p_j$), *T*)

if edge($p_i p_j$) is illegal
   then Let $p_i p_j p_k$ be the triangle adjacent to $p_r p_i p_j$ along edge($p_i p_j$).

   Legalize (p_r, edge($p_i p_k$), *T*)
   Legalize (p_r, edge($p_k p_j$), *T*)

The Delaunay Triangulation can be extended in three dimensions by defining edges, triangular faces or tetrahedrons containing the 3D point cloud to be analyzed, if there exists an empty sphere that passes through all the vertices [23].

A Voronoi diagram of a vertex set is a subdivision of the plane into polygonal regions, where each region is the set of points in the plane that are closer to some input vertex than to any other input vertex [21]. In other words, the vertices comprising the Voronoi

diagram lie at the center of the Delaunay triangles making up the triangulation surface (Figure 2.14).

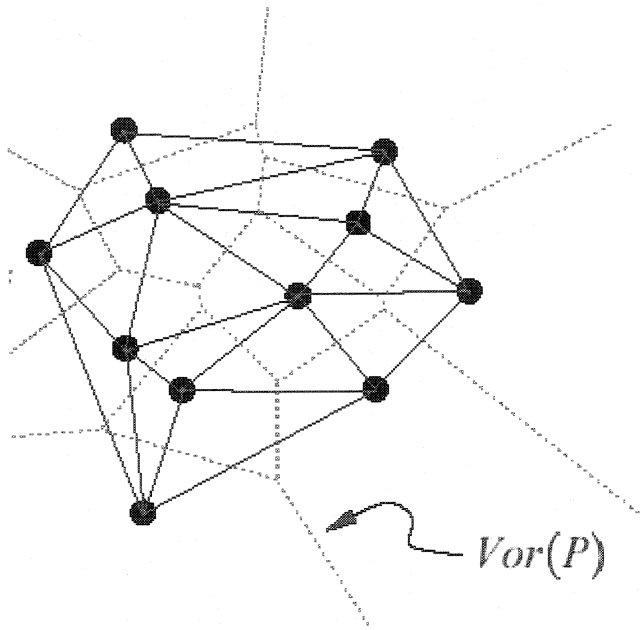

Figure 2.14 The Voronoi Diagram is the dual of the Delaunay triangulation [21].

We now have one way to represent a set of three-dimensional points as a volume. The problem with using the Delaunay triangulation is that for constructing the surface in 3D, the creation of tetrahedrons is imperative. This means that this approach relies on points inside the volume and this does not correspond well with data representing a cardiac chamber, which are mainly located over the endocardial surface.

2.8.2 The Voronoi- Based "CRUST" Approach of Amenta and Bern

This approach involves obtaining, as an end result, a region known as a *crust* out of a set of Voronoi vertices. In 2D, the algorithm described by Amenta and Bern is summarized as follows (Figure 2.15).

Definition: Let S be a finite set of points in the plane, and let V be the vertices of the Voronoi diagram of S. An edge between points *s1, s2* (both belong to S) belongs to the crust of S if there is a disk, empty of points in the union of S and V, touching *s1* and *s2*.

Therefore, the algorithm is simply as follows:

1) Let S and V be as stated above, and let S' be the union of S and V.

2) Let D be the Delaunay triangulation of S'.

3) An edge of D belongs to the crust of S if both its endpoints belong to S.

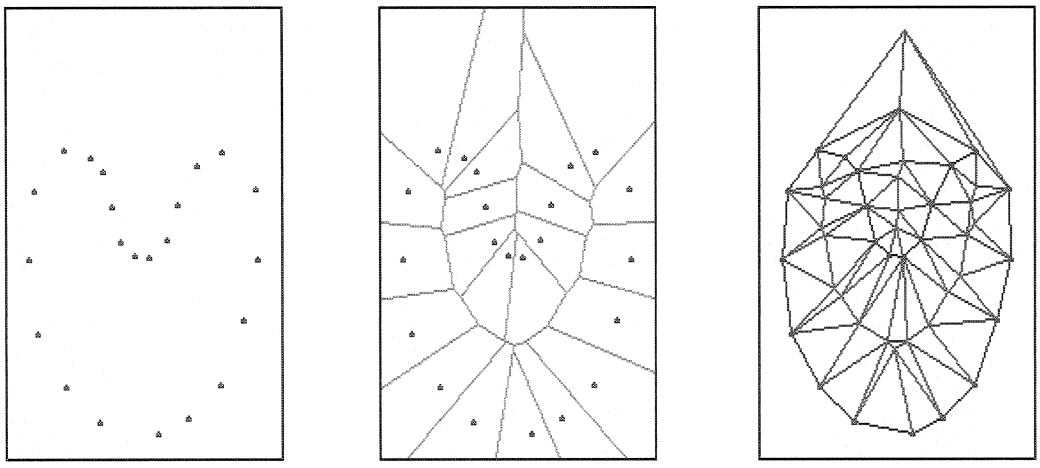

Figure 2.15 An unorganized point cloud in 2D (left), the corresponding Voronoi diagram (center) and the Delaunay triangulation (right). The *crust* is shown as the closed boundary inside the Delaunay diagram (right) [25].

The medial axis of a multidimensional surface in $\Re$ is (the closure of) the set of points with more than one closest point on the surface. Another definition would be that the medial axis consists of all points, which are centers of spheres that touch a given surface in at least two points. An example in $\Re^2$ is shown in Figure 2.16, and in $\Re^3$ in Figure 2.17. This definition of the medial axis includes components on the exterior of a closed surface. The medial axis is the extension to continuous surfaces of the Voronoi diagram, in the sense that the Voronoi diagram of S can be defined as the set of points with more than one closest point in S [26].

A difficulty with the extension of this algorithm to three dimensional coordinates is that, while in two dimensions the Voronoi vertices of a sufficiently dense data set are located near the medial axis, this is not necessarily the case in three–dimensional space.

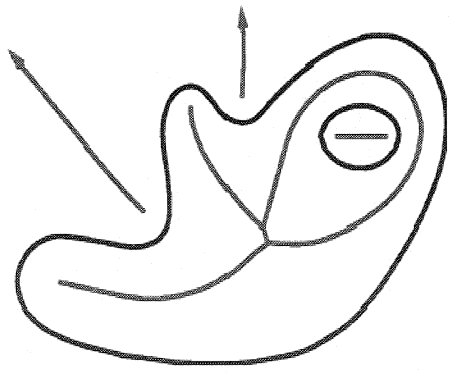

Figure 2.16 The light curves (red) are the medial axis of the heavy curves [26].

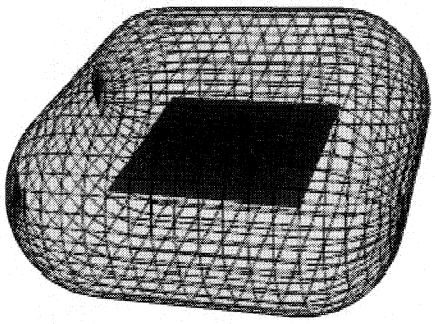

Figure 2.17 In 3D, the medial axis of a surface is generally a 2D surface. Here, the square is the medial axis of the rounded surface [26].

In order to obviate this difficulty, consider the Voronoi cell V_s of a sample s, as in Figure 2.18.

The procedure comprises the following steps.

1. For each sample point s:

(a) If s does not lie on the perimeter of the surface hull, let $p+$ be the farthest Voronoi vertex of V_s from s. Let $n+$ be the vector $sp+$.
(b) If s lies on the perimeter of the surface hull, let $n+$ be the average of the outer normals of the adjacent triangles.
(c) Let $p-$ be the Voronoi vertex of V_s with negative projection of $n+$ that is the farthest from s.

2. Let P be the set of all poles $p+$ and $p-$. Compute the Delaunay triangulation of $S \cup P$.

3. Retain only those triangles for which all three vertices are sample points in S.

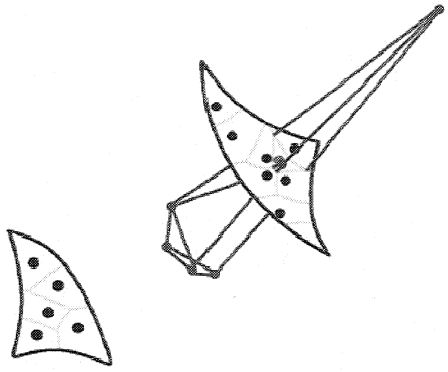

Figure 2.18 In 3D, The Voronoi cell, V_s, is long, thin, and roughly perpendicular to perimeter surface [26].

The crust usually does not describe a piecewise linear manifold. It may contain additional triangles that must be removed in a further filtering phase. The so-called normal filtering has been suggested where all triangles having normals deviating sign from n+ or n-. And remaining superfluous triangles are then eliminated in a final post–processing step [27].

2.8.3 The Growing Cell Structures Approach of Ivrissimtzis et al.

Ivrissimtzis, Jeong and Seidal [28] proposed a *Growing Cell Structures* algorithm, which displays flexibility and easiness in its adaptation to reconstructed volumes having odd shapes, concavities or complex features.

The network is the mesh that will be created depicting the surface, and its nodes are the mesh vertices. The information stored in a node is a 3D vector v, giving the position of that vertex, and a scalar value, called the signal counter, measuring the activity of that vertex during the adaptation process. In one step of the algorithm we sample our target space, which is a point cloud or an implicit surface, known here as a probability distribution. The sample is a single point s, seen here as a signal that will be processed by the neural network. We select the node of the network which is the nearest to the sample,

and we move that node and its direct topological neighbours towards the sample. This way the nodes move towards the target space, adapting their position to its geometry, as shown in Figure 2.19. Then, we update the signal counters of the nodes, increasing the counter of the best matching node to reflect its recent activity. The fact that only the best matching node and its topological neighbours respond to a signal can be seen as a kind of competition between the nodes and, traditionally, this kind of process is called competitive learning. Before deriving the algorithm, we begin by defining the environment where the nodes will be moved to optimal positions.

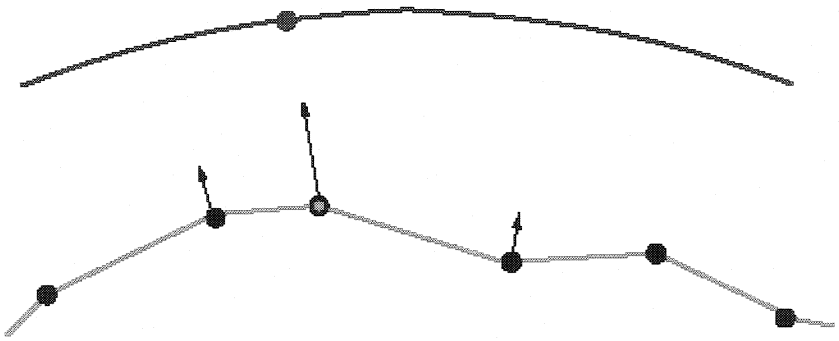

Figure 2.19 The target space (top line) with a solid circle as the signal sampled. The current state of the network (bottom line) contains nodes that move towards the signal and neighboring nodes will adjust their position [28].

Definition: Let M be denoted as the mesh. The set of network nodes, as well as the set of vertices of the mesh will be denoted as V. If $v \in V$ is a vertex, the signal counter measuring its activity will be denoted by τ_v. The mesh after one step of the iterations will be denoted as M'. A one-point sample from the target space will be denoted by s.

The algorithm is described as follows:

1. The target space is a point set which can also be seen as a probability distribution, by assigning to all the points an equal probability

$$p(v) = \frac{1}{|V|}, \qquad v \in V \tag{2.1}$$

2. Find the best-matching node of the network, that is, find the vertex v_w of M with the shortest distance to s.

3. Update the position of v_w and its direct topological neighbors. The update is a linear combination of the vertex and the sample s. Here, α_w is a constant.

$$v_w' = (1 - \alpha_w)v_w + \alpha_w s \tag{2.2}$$

The neighbor positions of v_w are also updated in order to improve the overall connectivity. For every v_i in the 1-ring of v_w the Laplacian L of v_i is measured by:

$$L(v_i) = \frac{1}{valence(v_i)} * \sum_{v_k \in 1-ring(v_i)} (v_k - v_i) \tag{2.3}$$

and we update M by a fraction of the tangential component of L.

$$L_t(v_i) = L(v_i) - (L(v_i) \cdot n)n \tag{2.4}$$

$$M' = M + \alpha_n L_t \tag{2.5}$$

where n is the approximated vertex normal of v_i and α_n is a constant.

4. After this processing of the sample of s, an update of the signal counter is made by:

$$\tau' v_w = \tau_{v_w} + 1 \tag{2.6}$$

and then we decrease the signal counter of all nodes by:

$$\tau'_v = \alpha\tau_v \qquad v \in V \tag{2.7}$$

where α is a constant. The signal counter gives an indication of how active a node happens to be, that is, how frequently it is the best matching node.

5. This section of the algorithm is called "every λ iterations" of the steps 1-4, where λ is a constant integer. We find the node with highest signal counter and perform a vertex split. Intuitively, the signal counter measures the activity of a vertex, and the most active vertices are in an area of the target space, which is currently under-represented by the nodes M. Thus, we perform a vertex split to create one more vertex in that area of the target space.

6. This last step in the *Growing Cells Structures* algorithm is defined as every $\mu \cdot \eta$ iterations of the steps 1-4, where μ is a constant integer and η is the number of nodes of the network. The nodes that have not been active in the last $\mu \cdot \eta$ iterations will be removed. The removal of redundant vertices is done by an edge collapse. Since an

edge collapse changes the valences of the incident triangles' vertices, the edge that gives the smallest regularity error is given by:

$$\frac{1}{3}\sqrt{(a+b-10)^2+(c-7)^2+(d-7)^2} \tag{2.8}$$

Where *a, b, c, d* are the valences of the vertices before the edge collapse (Figure 2.20)

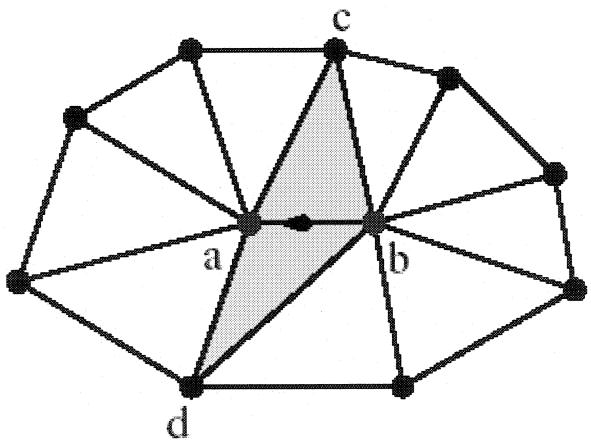

Figure 2.20 An edge with valence *a, b,* ends collapses, creating a vertex of valence *a + b - 4*. The two vertices opposite to that edge had valences *c, d*, before the collapse and have valences *c-1, d-1* after [28].

The *Growing Cells Structures* algorithm is stopped after a sufficient number of nodes are reached.

2.8.4 The Convex (Quick) Hull Approach of Barber et al.

Another classical method for reconstructing a 3D volume is that of the convex hull. The problem involves finding the smallest convex polygon containing all the points of *S*, given a set *S* of *n* points in multidimensional space [29].

The algorithm can be described briefly as follows for 2D points:

Select the farthest points (left and right) from the data set (2D) and draw a line between them. We examine a set of points lying on the same side of the line (CD). In this set, select the point E that is located furthest away from the line CD (Figure 2.21). This point will also belong to the convex hull, since it cannot be included in a triangle. Moreover, we can remove all the points inside the triangle (CDE), and split the remaining points in two subsets: one with the points on the left of the line (CE), and the other set containing points on the right of the line (CE). The iterative process is repeated in these two subsets. Once the outer shell of the hull is established, we can analyze the set of data points located under the line segment (CD) in the same manner.

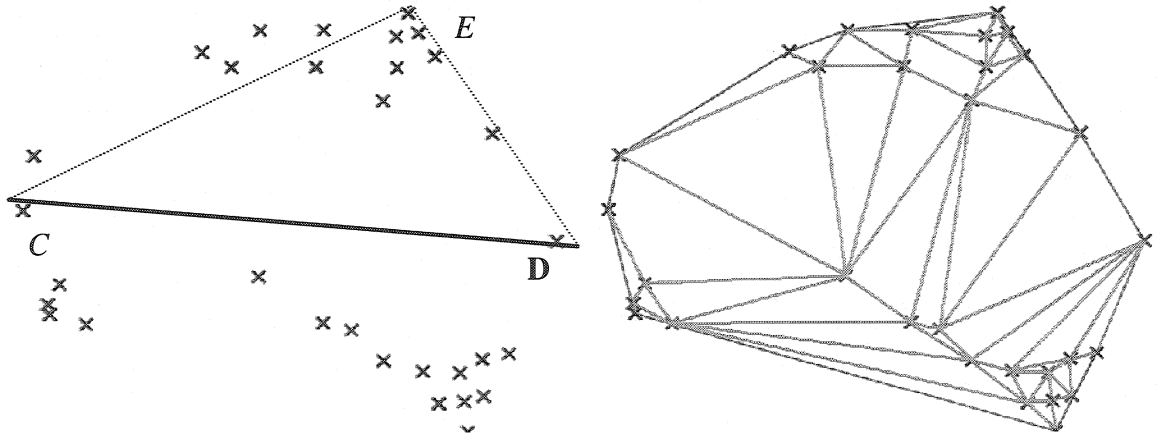

Figure 2.21 Convex Hull from a set of unorganized points

To expand this approach to three-dimension analysis, we replace the triangles by tetrahedrons. Unlike the Delaunay process, the tetrahedrons will not remain part of the volume. An initial tetrahedron is constructed, instead of a line in 2D, and points are searched and joined in a manner such that they are the most remote from each of the four triangular facets of the tetrahedron. Only the face of the triangle (from the tetrahedron) that will be part of the surface of the volume is retained. The remaining 3 faces of the tetrahedron are then eliminated.

The Convex Hull will have an empty interior (hull) and is the method of choice in our research. It is quick to implement and represents well the endocardial surface of cardiac chambers. Further, it was thought to be a good initial step to verify the feasibility of our approach.

2.8 Otsu's Automatic Thresholding Approach

Otsu derived a nonparametric and unsupervised method of automatic thresholding in 1979 [31]. This binary approach will seek the optimal threshold that will best separate the "two population" classes in an image (Figure 2.22). To better appreciate the significance of this widely used method, a description of the method is given here.

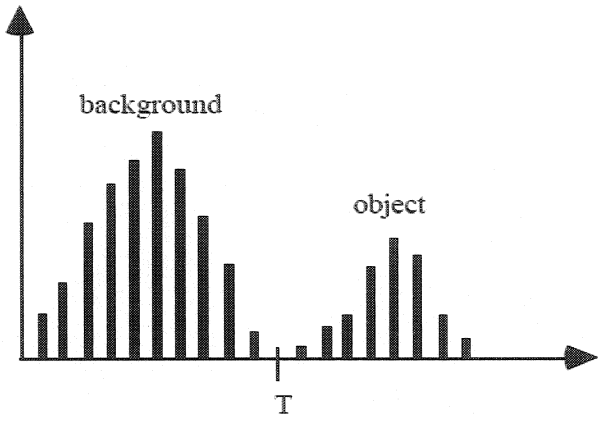

Figure 2.22 Gray level image intensity histogram and selection of threshold to separate the two classes of objects [30].

Let the pixels of a given picture be represented in L gray levels [1, 2,...L]. The number of pixels at level i is denoted by n_i and the total number of pixels by $N= n_1 + n_2 +... + n_L$. To simplify the derivation, we regard the gray-level histogram as a probability distribution with the following properties:

$$p_i = \frac{n_i}{N}, \quad p_i \geq 0, \sum_{i=1}^{L} p_i = 1 \tag{2.9}$$

If we divide the pixels into two classes C_o and C_1 (background and object), by assuming a threshold at k; C_o will signify pixels with levels [1,...,k], and C_1 will signify pixels with levels [k+1,...,L]. The probabilities for each class to occur is given by:

$$\omega_o = \Pr(C_o) = \sum_{i=1}^{k} p_i = \omega(k) \tag{2.10}$$

$$\omega_1 = \Pr(C_1) = \sum_{i=k+1}^{L} p_i = 1 - \omega(k) \tag{2.11}$$

We also define the class mean levels to be:

$$\mu_o = \sum_{i=1}^{k} i \Pr(i \mid C_o) = \sum_{i=1}^{k} \frac{ip_i}{\omega_o} = u(k) \Big/ \omega(k) \tag{2.12}$$

$$\mu_1 = \sum_{i=k+1}^{L} i \Pr(i \mid C_1) = \sum_{i=k+1}^{L} \frac{ip_i}{\omega_1} = \frac{\mu_T - \mu(k)}{1 - \omega(k)} \tag{2.13}$$

where:

$$\omega(k) = \sum_{i=1}^{k} p_i \tag{2.14}$$

$$u(k) = \sum_{i=1}^{k} ip_i \tag{2.15}$$

are the 0^{th} and 1^{st} order cumulative moments of the gray-level histogram up to the kth level. The total mean of the original image can be defined as:

$$\mu_T = \mu(L) = \sum_{i=1}^{L} i p_i \tag{2.16}$$

The following relation can be verified for any threshold level k of choice:

$$\omega_o \mu_o + \omega_1 \mu_1 = \mu_T, \quad \omega_o + \omega_1 = 1 \tag{2.17}$$

The pixel class variances are given by:

$$\sigma_o^2 = \sum_{i=1}^{k} (i - \mu_o)^2 \Pr(i \mid C_o) = \sum_{i=1}^{k} (i - \mu_o)^2 \, p_i \Big/ \omega_o \tag{2.18}$$

$$\sigma_1^2 = \sum_{i=k+1}^{L} (i - \mu_1)^2 \Pr(i \mid C_1) = \sum_{i=k+1}^{L} (i - \mu_1)^2 \, p_i \Big/ \omega_1 \tag{2.19}$$

The above variances will require the computation of second order statistical moments. To determine the optimal threshold level, Otsu first introduced the following discriminant measures for class separability:

$$\lambda = \sigma_B^2 \Big/ \sigma_W^2, \quad \kappa = \sigma_T^2 \Big/ \sigma_W^2, \quad \eta = \sigma_B^2 \Big/ \sigma_T^2 \tag{2.20}$$

where σ_W^2 is the within-class variance, σ_B^2 is the between-class variance, and σ_T^2 is the total variance of levels, computed from :

$$\sigma_W^2 = \omega_o \sigma_o^2 + \omega_1 \sigma_1^2 \tag{2.21}$$

$$\begin{aligned} \sigma_B^2 &= \omega_o (\mu_o - \mu_T)^2 + \omega_1 (\mu_1 - \mu_T)^2 \\ &= \omega_o \omega_1 (\mu_1 - \mu_o)^2 \end{aligned} \tag{2.22}$$

$$\sigma_T^2 = \sum_{i=1}^{L} (i - \mu_T)^2 p_i \tag{2.23}$$

The problem consists of finding the threshold that gives the best separation of classes. The discriminant criteria κ, η are related to λ by $\kappa = \lambda + 1$ and $\eta = \lambda / (\lambda + 1)$ because of the following relation:

$$\sigma_W^2 + \sigma_B^2 = \sigma_T^2 \tag{2.24}$$

We note that the within-class variance and the between-class variance are both functions of the threshold k, but the total variance is independent of k. We also note that the within-class variance is based on second-order statistics while the between-class variances is based on first order statistics. Hence, the simplest measure with respect to the threshold is η, and Otsu uses this measure to calculate the optimal threshold k^*. The optimal threshold maximizes η, and hence maximizes the between class variance in equation (2.22). It is selected by using equation (2.12) and equation (2.13):

$$\eta(k) = \sigma_B^2(k) / \sigma_T^2 \tag{2.25}$$

$$\sigma_B^2(k) = {[\mu_T \omega(k) - \mu(k)]^2} \Big/ {\omega(k)[1 - \omega(k)]} \tag{2.26}$$

and the optimal threshold k^* will be:

$$\sigma_B^2(k^*) = \max_{1 \le k \le L} \sigma_B^2(k) \tag{2.27}$$

Otsu's procedure uses the 0^{th} and 1^{st} order cumulative moments of the gray-level histogram.

Chapter 3

Biplane Analysis

In this chapter, we develop and test a mapping technique based on biplane measurements of electrode sites and on the reconstruction of the cardiac chamber with the Convex Hull algorithm. An animal experiment was carried out to obtain the required fluoroscopic images and electrograms from the right and left ventricles so that a realistic 3D volume of the heart could be created.

3.1 Data Acquisition

3.1.1 Experimental Protocol

An animal experiment was carried out at Sacré Coeur Hospital. Our experimental protocol met the institutional requirements of animal experimentation. A mongrel dog was anesthetized and laid on its right side on a fluoroscopy table (*Integris Allura, Philips Inc.).* A reference catheter and a pacing catheter were inserted into the right ventricle, close to the septal wall. The role of the reference catheter was to define an origin for our 3D coordinate system that is not affected by the displacement of the heart due to respiration or by the displacement of the animal or the x-ray system. The role of the pacing catheter was to produce a simple electrical activation sequence so as to validate the isochronal maps. Finally, a standard 7-French RF ablation catheter was inserted from the femoral vein into the left ventricle of the dog.

During the course of the experiment, this mapping catheter was moved to 20 different sites (point-by-point) within the ventricle in order to obtain electrical and geometrical data from sufficient sites to map the activation sequence. Bipolar electrograms were recorded with the mapping catheter and the reference catheter using a multi-channel

analog-to-digital (A/D) converter card (*PCI DAS-1001, Omega Engineering Inc.*). The electrograms were saved in text file format.

The X-Ray images were obtained with the *Integris Allura Philips* fluoroscope. An advantage of this fluoroscope is the effective reduction of the dosage of X-rays by the use of pulsed emission and by an advanced filtration system of soft radiations [19]. The fluoroscopic image acquisition rate was set at 60 frames/second and images were recorded for about 2 seconds at the end of the expiration. This was achieved by stopping the respirator. The monoplane fluoroscopic C-arm was rotated by 90^0 to acquire two images for each mapping site: a left lateral view (the C-arm in a vertical position) and a posterior view (the C-arm in a horizontal position). Images were recorded, in Dicom format, (Figure 3.1) with a 512 x 512 pixel resolution.

In the end, the data collected totaled twenty posterior view images, twenty left lateral view images and the twenty electrograms.

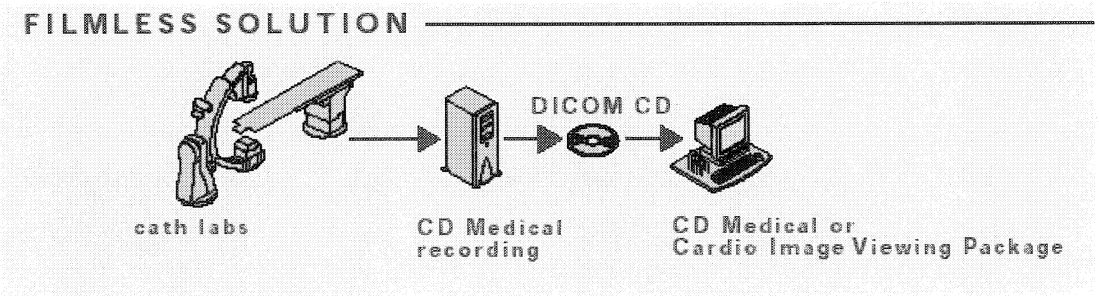

Figure 3.1 Data Acquisition Sequence between fluoroscope and PC [20].

3.1.2 Electrical Activation Time Measurements

The bipolar electrograms recorded during the experiment were analyzed as follows. The electrograms obtained from both the mapping and pacing catheters were saved together in the same text file. With the aid of a graphical user interface created in MatLab, we selected, using a cursor, the points of maximum negative slope on the two electrograms. Both must have visible negative slopes to obtain an accurate measure of the activation time. Hence, by placing the cursor on A (reference electrogram) and then on B (mapping catheter electrogram), the activation time was calculated by taking the difference of those two time values. For example, in Figure 3.2, the activation time is 78 ms.

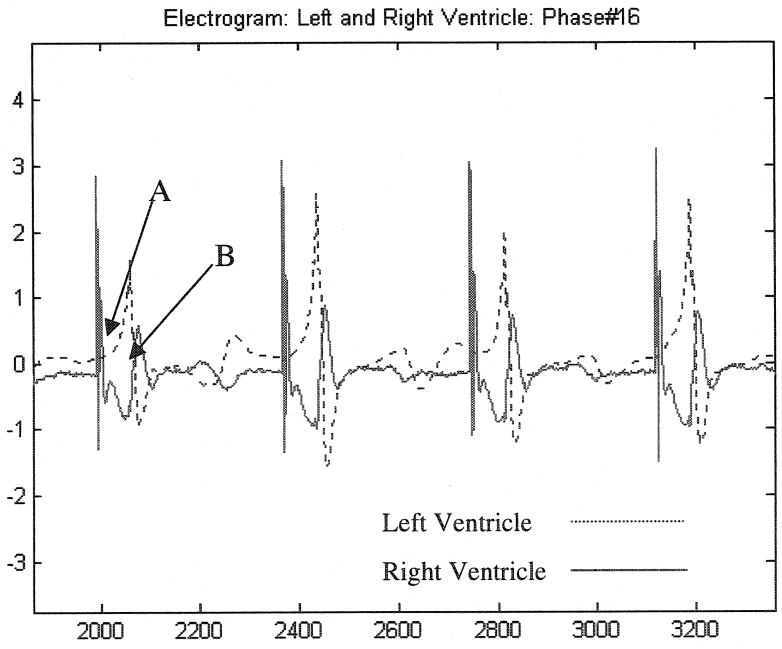

Figure 3.2 Electrograms from pacing (right ventricle) and mapping catheters

3.1.3 Fluoroscopic Image Analysis

So as to minimize motion blur, we developed the following algorithm to select the frame for each mapping site. The number of frames making up each sequence varied depending on how long the technician stepped on the pedal. In general, each sequence contained between 100-200 frames. By calculating the standard deviation of the differences between all the pixels of two successive frames, we were able to determine that the frame showing the smallest standard deviation also had the least motion blur (Figure 3.3). This frame represents the diastolic phase of the cardiac cycle. The maximum standard deviation occurred during the systolic phase. Once all 40 sequences were analyzed in this manner, the 40 diastolic frames were extracted to Jpeg format.

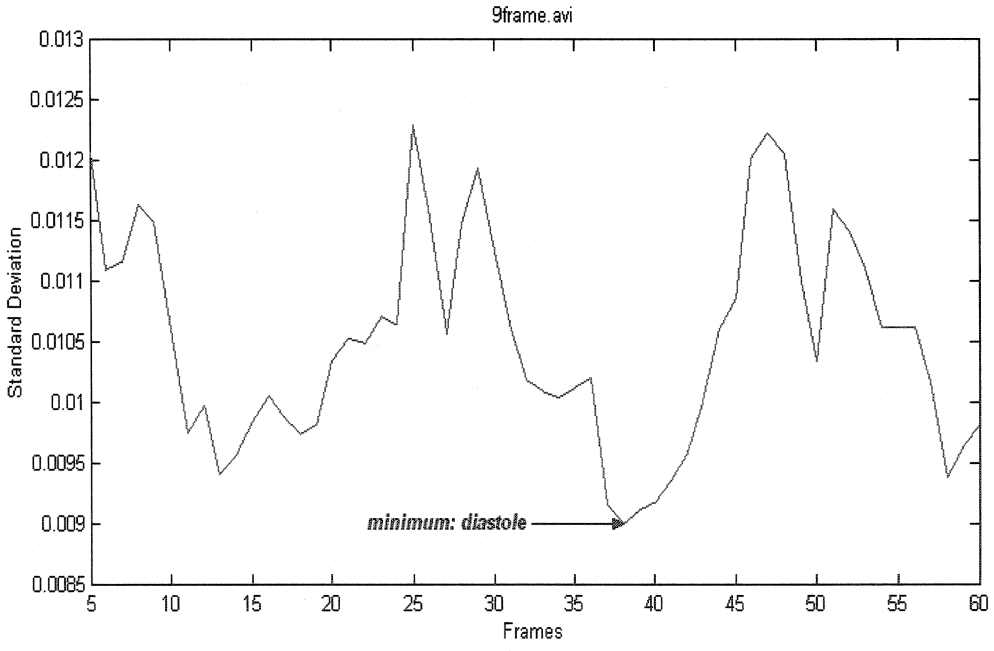

Figure 3.3 Standard deviation of the differences between successive frames during a one second sequence (60 frames). Shown here is a zoom between frames 5-60 taken from posterior view image #9.

3.1.4 Tip Electrode Coordinate Measurement

A right-handed coordinate system was centered on the tip of the reference catheter (Figure 3.4). MatLab's Image Processing Toolbox 4.0 was used for imaging processing. An algorithm was developed to measure the location of the tip electrode of the reference and mapping catheters (Figure 3.5). First, the images were manually cropped around the catheter tip. These grayscale images were converted into binary ones (black and white) using automatic thresholding (Otsu's method).

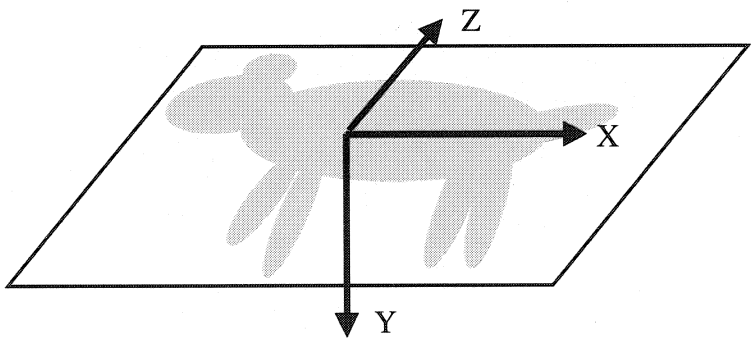

Figure 3.4 Right-handed coordinate system centered on the tip of the reference catheter. Posterior View: *XY* plane; Left Lateral View: *XZ* plane

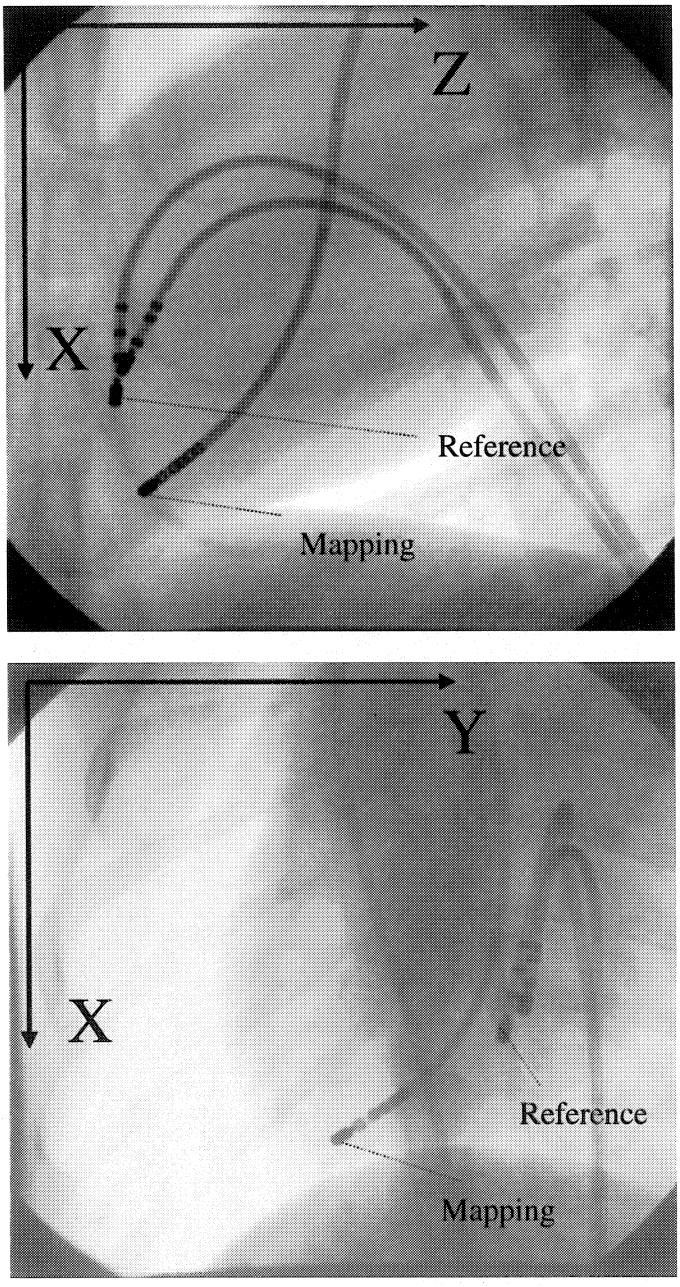

Figure 3.5. Diastolic frames for left lateral view (top) and posterior view (bottom), with associated coordinate representation

The centroids of the electrodes were then calculated (*regionprops* function) so as to obtain the coordinates required for each of the two views (XY and XZ). We observed a small difference (about 4 pixels) between the X coordinates of the same electrode seen on the two perpendicular views. Thus, we assumed a perfect biplane acquisition by retaining only the X value from the XY image. This process completed, we then had a set of three-dimensional coordinates reflecting the positions of the mapping electrodes. Finally, we subtracted the coordinates of the reference catheter for each mapping site so as to compensate for respiration and motion artifacts. These values were coupled with the respective activation times and saved in text file (Figure 3.6).

X	Y	Z	Time (ms)
78	-124	24	73
19	-43	98	56
-35	-126	218	79
-126	9	196	86
-156	-72	197	76
6	-48	231	67
5	-82	43	70
-58	-157	96	72
-143	-68	178	82
50	-134	33	77
-54	-6	130	68
-3	-17	166	61
-149	-20	179	88
-142	-58	236	98
-129	-82	216	94
3	-113	150	78
38	-68	71	65
-72	3	158	60
-99	-108	188	81
51	-136	43	74

Figure 3.6 Corrected XYZ coordinates (pixels) and local activation times (ms) for each of the 20 mapping sites in the left lateral view

3.2 Experimental Results

3.2.1 3D Convex Hull of Left Ventricle

Using the results of Figure 3.6, we applied the 3D Convex Hull algorithm using the *convhulln* function in MatLab to obtain the volume shown in Figure 3.7. We notice that a single point is located inside the Convex Hull and that the 19 other points are on the reconstructed surface. The single point inside the 3D volume is probably due to the concavity of the left ventricle. After creating the 3D convex hull, the electrical activation times measured at each node were linearly interpolated over the surface of this volume and displayed as a color shift, using red for the earliest activation times and blue for the latest.

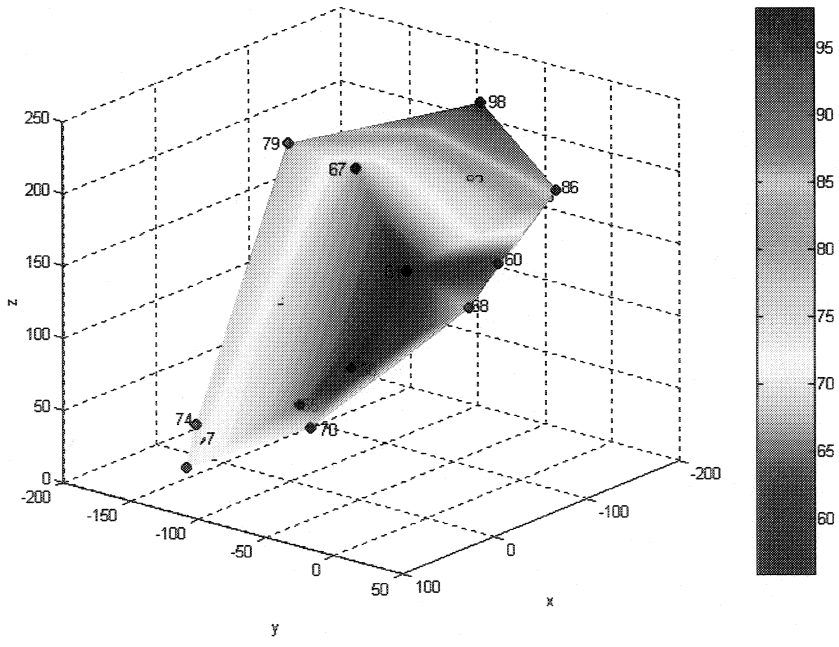

Figure 3.7 Convex Hull of left ventricle with associated activation times (in ms)

3.2.2 Fusion of the 2D Isochronal Maps onto Fluoroscopic Images

So as to plot only the triangles that can be seen from a certain point of view, the normal to the surface of each triangle was calculated (the normal points outward), and if its dot product with the observation point vector was positive, the triangle was retained. For example, for the posterior view (XY plane), we retained all the nodes associated with a triangle whose normal component in the Z direction is positive. Similarly, for the left lateral (XZ) plane, we retained the nodes associated with a triangle whose normal component in the Y direction is negative.

The fusion between the 2D isochronal activation map and the fluoroscopic image was performed in a 6-step process, as outlined below:

1. The nodes visible from the given point of view are identified using the Convex Hull data, and their 2D coordinates are retained (for example, for the posterior view, the nodes are in the XY plane).
2. The activation times of the visible nodes are positioned in a matrix, at the 2D coordinate locations of the nodes (*linspace* and *meshgrid* functions).
3. The Delaunay method is used to organize the set of visible points as a set of triangles and cubic interpolation is applied to interpolate the activation times inside each triangle (*griddata* function).
4. In order to fuse the isochronal map to the [512x512] size fluoroscopic image, the borders of the above matrix are completed with zeros to achieve the same size as the image.
5. The values of the [512x512] activation time matrix are scaled so that the maximum value is equal to 64 (which correspond to blue) and the minimum value is equal to 0 (which correspond to red).
6. The scaled activation time matrix is used to create an RGB color matrix (using a red-to-blue color map), which is finally plotted over the fluoroscopic image with a

30% transparency ratio (30% for the color isochronal map and 70% for the grayscale fluoroscopic image).

We also developed a more dynamic display of the cardiac activation sequence which is displayed on the computer screen as a movie with colored isochronal regions appearing over the fluoroscopic image as the electrical activation progresses during the cardiac cycle. The scaled [512x512] activation time matrix is then used to create eight [512x512] matrices which retain, respectively, the scaled activation times between 0 to 8, 9 to 16, 17 to 24, etc. The first matrix corresponds to a red shade; the second, to orange; the third, to yellow, etc. Each of those matrices are converted to RGB format and plotted in turn over the fluoroscopic image with a 70% transparency ratio.

The superposition of the 2D isochronal map over its associated fluoroscopic image is illustrated in Fig. 3.8. The reference catheter is marked with an "X". Earliest activation times are clearly closest to the stimulation catheter (near the reference catheter). The posterior view also shows that the isochronal map followed the contour of the mapping catheter, which corresponds to the contour of the left ventricular cavity.

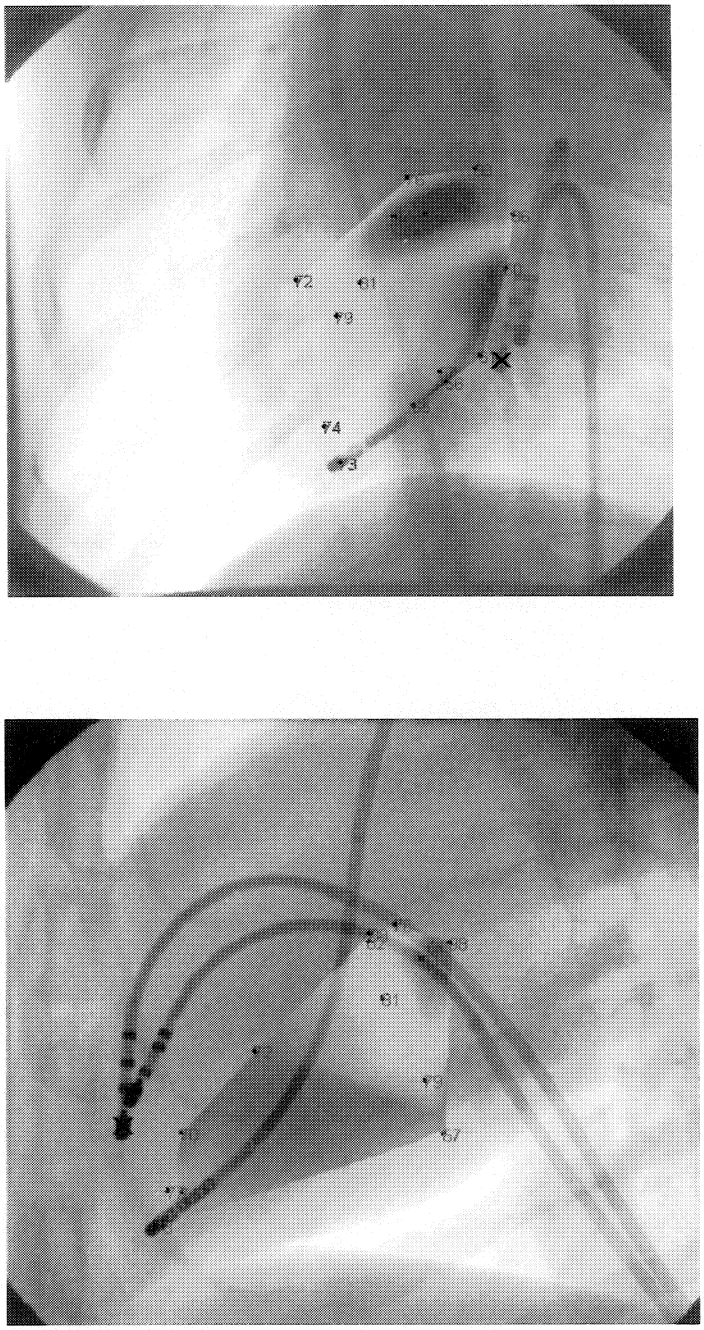

Figure 3.8 Fusion of isochronal activation map on the posterior view of the canine heart (top) and on the left lateral view (bottom).

Chapter 4

Monoplane Analysis

True biplane fluoroscopy systems are rare because of their relatively high cost. Also, obtaining two projections by rotating the C-arm of a monoplane fluoroscopy system at each mapping site as we did in our study is cumbersome and time consuming. Thus, there is a real need for computing the depth of the catheter tip from a single image.

Theoretically, the depth of the tip electrode can be obtained from the width of its image as the projection of an object becomes larger as it approaches the x-ray source. In Figure 4.1, the variable *b* represents the distance from the source to the surface of its enclosure, *z* is the distance between the surface of the enclosure and the electrode, *a* is the total distance between the source and the fluoroscopic plate, *c* is the electrode width and *w* is the width of the projection of the electrode.

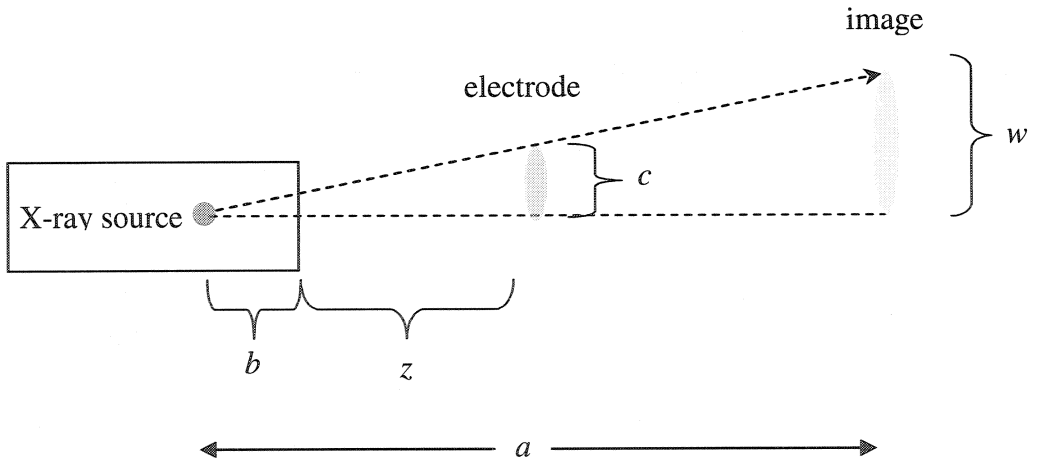

Figure 4.1 Geometric model relating the size of the electrode projection and various distances from the fluoroscopic source.

Geometric proportionality permits us to define the following equation:

$$\frac{c}{w} = \frac{b+z}{a} \tag{4.1}$$

from which we deduce that the inverse of the projection width w is proportional to the distance z:

$$\frac{1}{w} = \left(\frac{1}{ac}\right)z + \left(\frac{b}{ac}\right) \tag{4.2}$$

In this chapter, image-processing procedures were developed to determine the pixel width of the projection of the tip electrode (w) and tested to estimate the electrode depth (z). Testing was carried out for two experimental situations: the catheter was either displaced at known distances in the air, or the experimental data from the preceding chapter was used.

4.1 Binary Image Thresholding

Our first method relied on the conversion of the grayscale image of the catheter to a black-and-white image from which the width of the tip electrode region was measured. The posterior and left lateral images were first complemented and the contrast was improved by altering the grayscale values so as to stretch the histogram (MatLab function: *imadjust*). We manually cropped the image around the catheter tip. The cropped grayscale image was converted to a binary image using two related approaches that are described in this section. Then, we manually selected the region of the tip electrode amongst the different white objects within the small window. The width was estimated from the minor axis of the ellipse having the same second-moment (Figure 4.2) as the electrode region (Matlab function: *regionprops, minor axis*).

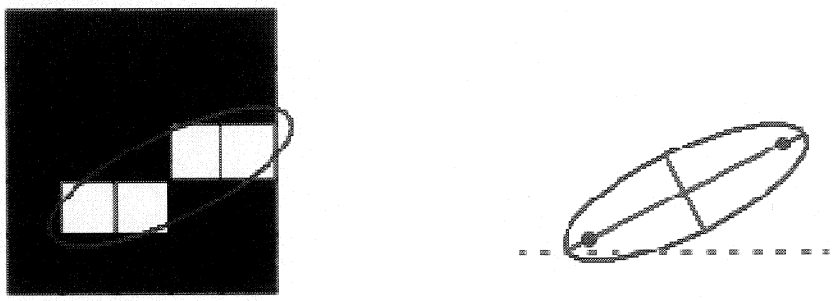

Figure 4.2 An ellipse having the same second-moment as the binary region is used to estimate the width of the tip electrode from the minor axis of the ellipse [5].

The conversion of a grayscale image to a binary image can be performed using a simple threshold. This requires the user to manually set a threshold value dividing the image intensities into two classes. This manual approach is generally not appropriate because of the variation in contrast from image to image which requires repeated changes in the threshold, which is time consuming and generates variability in the results. Therefore, we also implemented Otsu's automatic thresholding approach as described at the end of the literature survey in Chapter 2.

4.2 Projection Method with prior Morphological Filtering

The width estimated with the thresholding method is an approximation because the tip electrode is not an ellipse. We developed an alternative approach, which is based on the projection of the grayscale image along a line perpendicular to the electrode tip. The cropped grayscale image is rotated to the vertical position and the values of each pixel belonging to a given column of the rotated image are added together for every column. This projection results in a bell-shaped curve (Figure 4.3, top) from which the tip electrode width can be measured. However, objects in the background around the electrode tend to blur the projection and to widen the apparent width of the tip electrode.

Thus, we had the idea of filtering the image so as to obtain a black background. The projection of the filtered image then results in a thinner bell shape curve (Figure 4.3, bottom). We used the morphological filtering approach to eliminate the background.

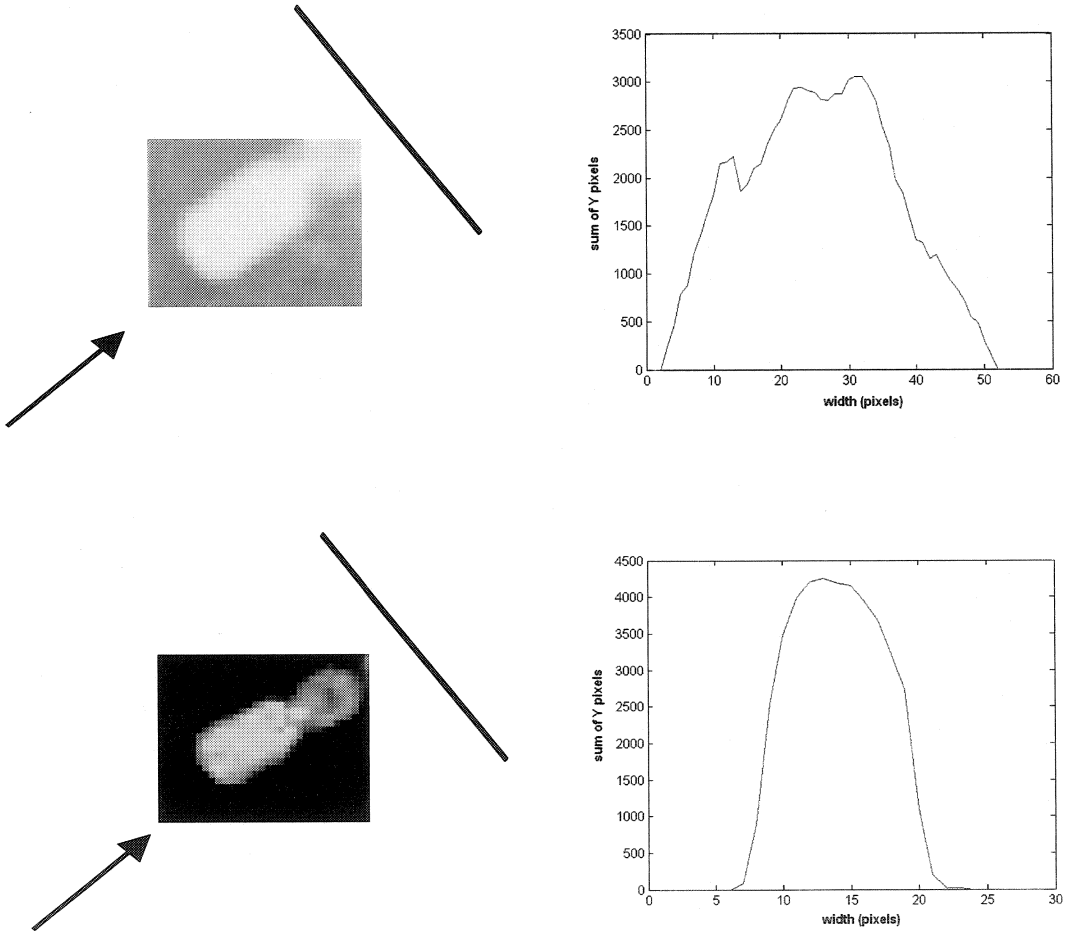

Figure 4.3 Grayscale image of tip electrode with bell shape projection (top). By eliminating the background with a morphological filter, the projection improves (bottom)

Morphological filtering is particularly useful in analyzing grayscale and binary images and is of common usage for edge detection, noise removal, image enhancement and image segmentation [32]. In our research, the object of interest is the electrode at the end of the catheter. We need to isolate this object and eliminate neighborhood objects from our analysis to estimate the width of the tip electrode. The solution to this problem is obtained by applying a test to the elements (or objects) present in the image being analyzed and verifying how each reacts to this test. This involved the creation of a *structuring element* that passes through the entire image window and interacts with every element in it. Two-dimensional, or flat, structuring elements consist of a matrix of 0's and 1's, typically much smaller than the image being processed. The center pixel of the structuring element, called the origin, identifies the pixel of interest — the pixel being processed. The pixels in the structuring element containing 1's define the neighborhood of the structuring element. Examples of structuring elements are: disk, ball, diamond (Figure 4.4), rectangle, lines, etc.

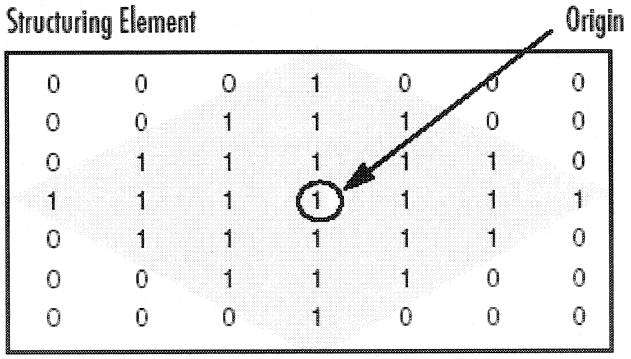

Figure 4.4 Diamond-shape structuring element [33].

The two basic mathematical operators that we used in our morphological filtering were *dilation* and *erosion.*

Dilation refers to the adding of pixels to the boundaries of objects in a black and white image. For grayscale images, the value at the point of interest of the filtered image is set

to the highest value of the original image within the boundaries of the structuring element around the point of interest. For example, the top of Figure 4.5 shows cross-sections through a grayscale image and its filtered version using a disk shaped structuring element [34]. Grayscale dilation with a flat disk shaped structuring element will generally brighten the image. Bright regions surrounded by dark regions grow in size, while dark regions surrounded by bright regions shrink in size. The effect is most striking at places in the image where the intensity changes rapidly and regions of fairly uniform intensity are largely unchanged except at their edges.

On the other hand, *erosion* refers to the process of removing or eliminating pixels on the boundary of objects in a black and white image. Grayscale erosion consists of assigning at the point of interest of the filtered image, the lowest value of the original image within the boundaries of the structuring element (Figure 4.5 bottom). Erosion with a flat disk shaped structuring element will generally darken the image and small bright spots disappear as they are eroded down to the surrounding intensity value [35].

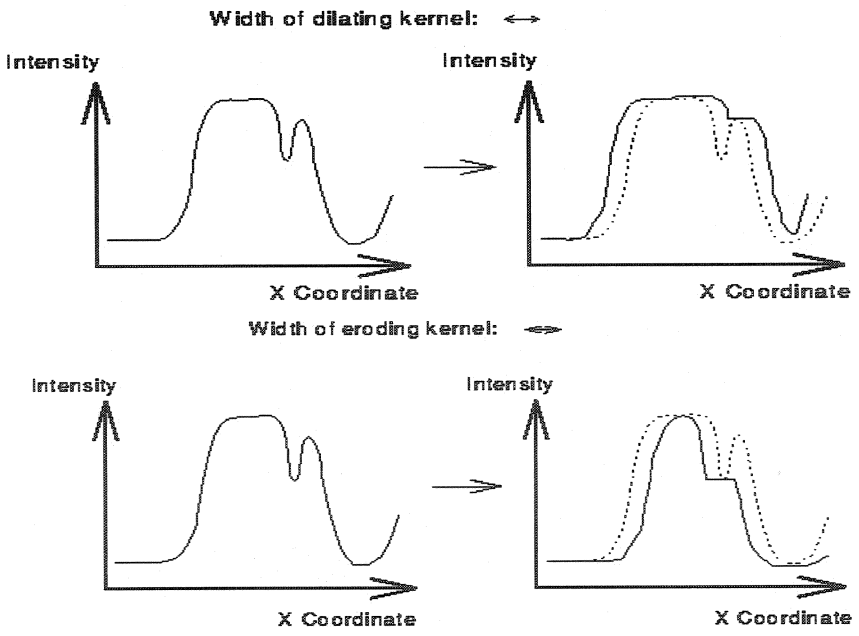

Figure 4.5 Grayscale dilation (top) and erosion (bottom) using a disk shaped structuring element. The graphs show a vertical cross-section through a grayscale image [34, 35].

The two fundamental operators discussed above constitute the basis of the algorithm implemented to estimate the tip electrode width. Dilation and erosion are successively applied to the image to form a new morphological operator known as *opening*. The basic effect of an opening is somewhat like erosion in that it tends to remove some of the bright pixels from the edges of regions of foreground pixels. However it is less destructive than erosion in general. As with other morphological operators, the exact operation is determined by a structuring element. The effect of the operator is to preserve foreground regions that have a similar shape to this structuring element, or that can completely contain the structuring element, while eliminating all other regions of foreground pixels [36].

We subtracted from the cropped image, an image that was morphologically filtered by an opening operation using either a ball, a disk or a diamond as the structuring element [33]. This opening operation eliminated the tip electrode while preserving the background, thus, by subtracting this filtered image from the original image, the catheter was retained while the background was eliminated (Figure 4.3, bottom).

Second, the tip electrode region was rotated to a vertical position. The rotation was accomplished by first automatically converting the cropped image into binary form. With the aid of a cursor we selected the tip electrode region and the rotation angle was automatically calculated with the *regionprops, orientation* MatLab function. The cropped grayscale image was then rotated to the vertical position using the *imrotate* function. The values of each pixel belonging to a given column of the rotated image were added together, and this was repeated for every column so as to project the image along its base. This projection resulted in a bell-shaped curve (Figure 4.6). Finally, a threshold was fixed at 50% of the maximum of this curve (a more robust analysis); the two interception points of the bell-shaped curve with the threshold were calculated by linear interpolation (L_1 and L_2) to estimate the width of the electrode. An important aspect of this method is that this width estimate is not an integer value of the pixel size of the image.

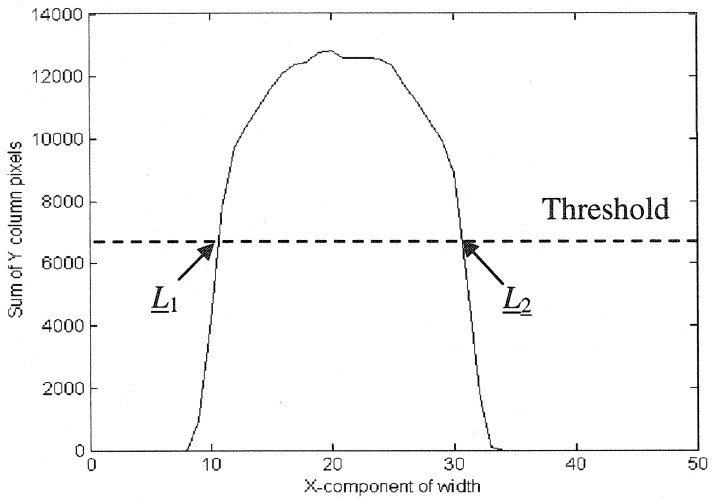

Figure 4.6 Projection Algorithm: bell shaped curve representing the projection of the tip electrode from a grayscale image whose background was morphologically filtered.

Once the projection was made and the estimated width was calculated, another problem surfaced. We needed to be certain that the tip electrode was actually in a vertical position (90^{o}). We know that the elongated electrode should have a smaller width in a truly

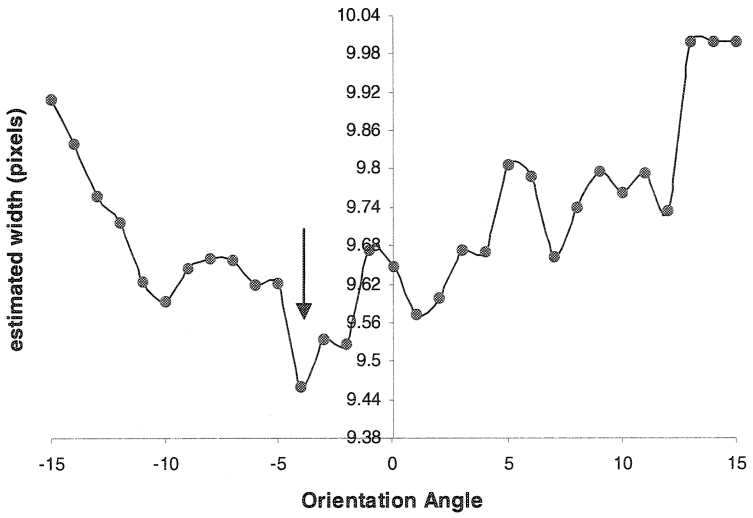

Figure 4.7 Estimated widths versus orientation angle.
Arrow indicates minimum value

vertical position than if it were positioned at a slight angle. A simple solution for this problem is to estimate the width for orientations other than the initial estimate of the vertical position within a given range (for example, every 1° within ±15° of the original estimate) and to retain the smallest value (Figure 4.7).

4.3 Catheter in Air Displacement Experiment

An initial experiment was performed using a catheter that was positioned over a radiotranslucent cardboard box and displaced at 1 cm increments away from a fluoroscopic source.

First, we illustrate the results obtained with a manually selected threshold of 0.16 (which provided the best results here). An example of binary image is shown in Figure 4.8.

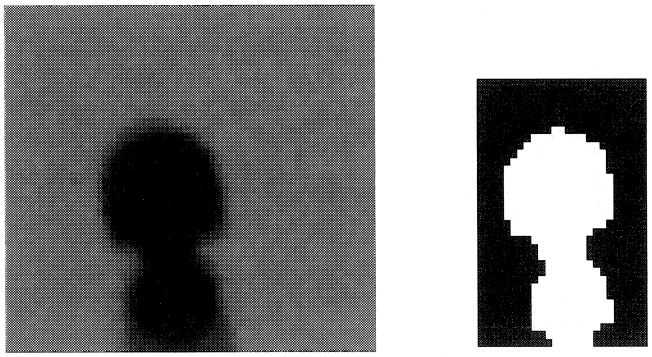

Figure 4.8 Grayscale image of tip electrode in the air (left) with cropped binary image (right).

Figure 4.9 shows the data obtained in the air experiment using manual thresholding (top) and automatic thresholding (bottom). As established in equation (4.2), the inverse of the projection width w is plotted as a function of the depth z. A linear regression line passes through the data points.

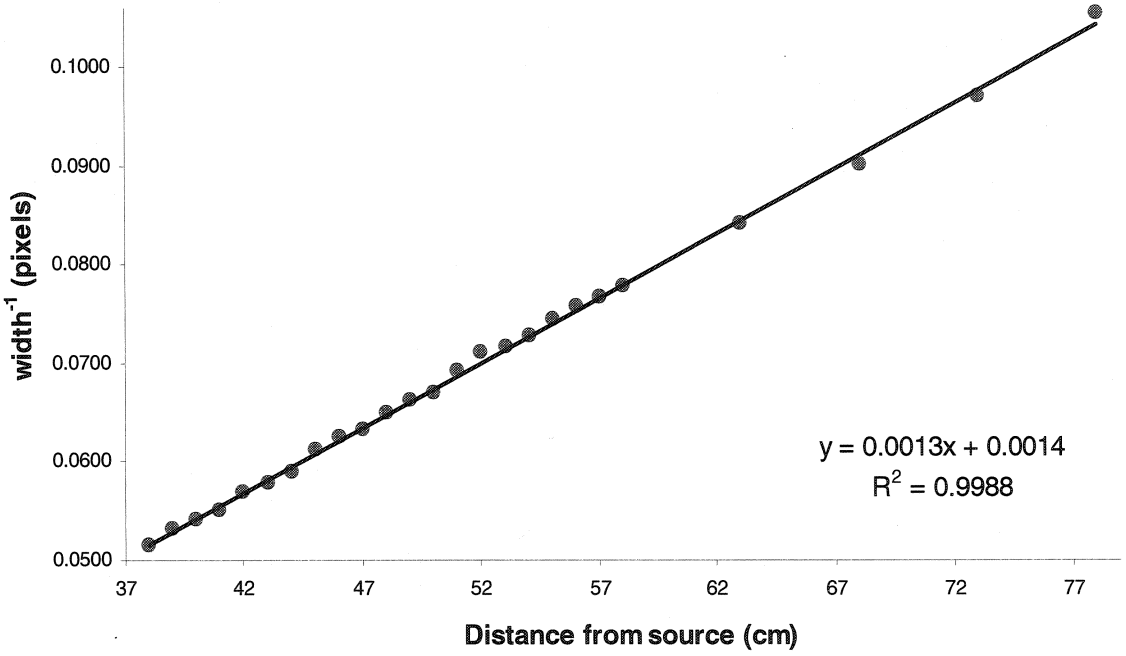

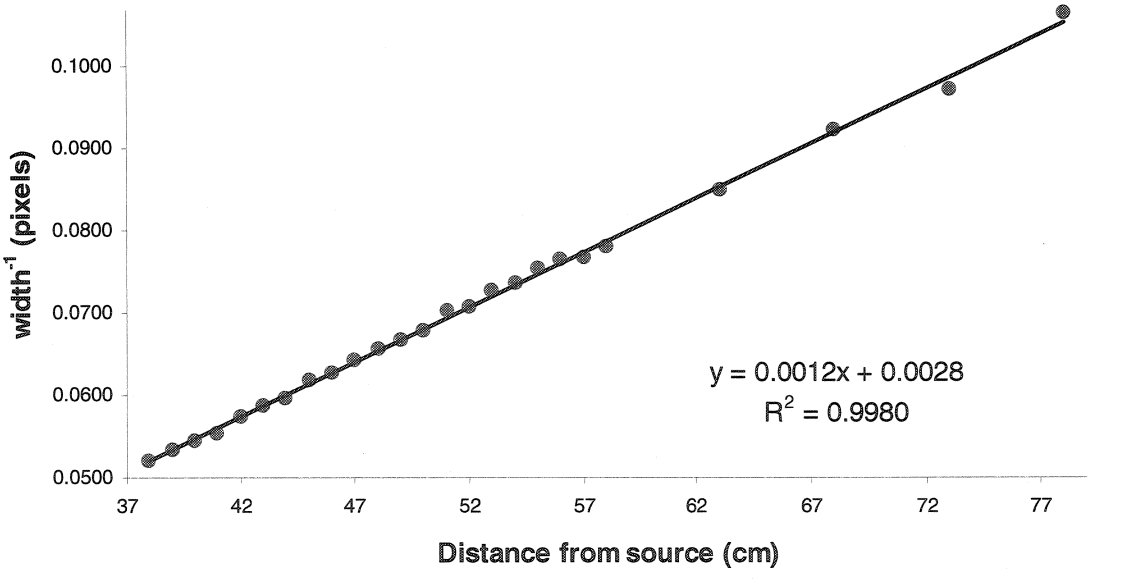

Figure 4.9 Inverse of the projection width *w versus* depth *z* for the manual thresholding approach (top, threshold=0.16), and the automatic thresholding approach (bottom).

The results from Figure 4.9 indicate an almost perfect correlation. The correlation coefficient was *r=0.9988* for the manual thresholding approach, and *r=0.9980* for automatic thresholding. To evaluate the accuracy of the monoplane approach for the estimation of the depth, we estimated the tip electrode depth from the tip electrode width using the regression line shown in Figure 4.9. The standard error of estimate for the manual thresholding approach was SE = 3.6 mm and for the automatic thresholding approach it was SE = 4.7 mm.

4.3.1 Results of the Thresholding Approach for Canine Fluoroscopic Images

The quality of the results deteriorated significantly when passing from the air setup to the animal setup. With the manual thresholding approach (threshold = 0.16), the correlation coefficient was r = 0.38 for the lateral view whereas the widths measured in 8 of the 20 images for the posterior view were grossly overestimated. With the automatic threshold approach, the correlation coefficients (Figure 4.10) were r = 0.51 for the left lateral view (p<0.05) and r = 0.17 for the posterior view (r is statistically not significant). The standard error of estimate for the depth computed from the width was 44 pixels for the left lateral view analysis and 69 pixels for the analysis of the posterior view.

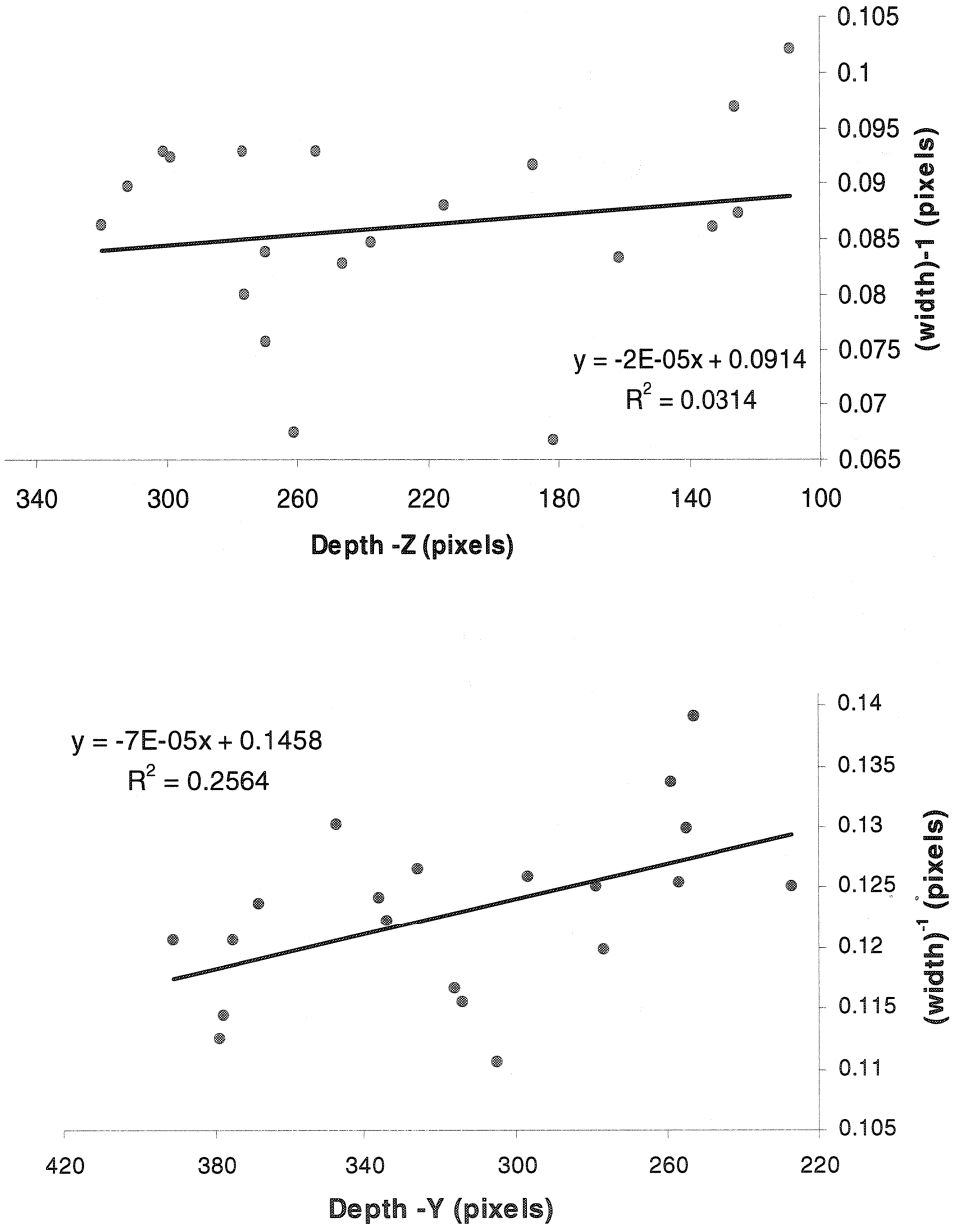

Figure 4.10 Results for automatic thresholding in the canine experiment. Inverse of tip electrode width versus depth in the posterior view (top, -Z) and the left lateral view (bottom, -Y)

4.3.2 Results for the Projection Approach

We proceeded with three sequences of analysis by rotating the images within 90 ± 5^0, 90 ± 10^0, and 90 ± 20^0 as described in section 4.2. We initially selected only the posterior fluoroscopic images for our analysis because these provided the worst results for the automatic thresholding approach.

The correlation coefficient for a rotation range of $\pm5^0$ was $r = 0.39$, and the standard error of estimate was 67 pixels. For a rotation range of $\pm10^0$, the correlation coefficient was $r = 0.47$ with a standard error of estimate of 65 pixels. Finally, a correlation coefficient of $r = 0.44$ and a standard error of estimate of 67 was obtained for a rotation range of $\pm20^0$. These correlation coefficients are all statistically significant ($p<0.05$).

These results demonstrated that there was no significant difference between rotating the image by $\pm10^0$ or $\pm20^0$. At this stage, the decision was made to implement the morphological filtering and projection algorithm by rotating each image within $\pm20^0$ from its vertical position,. We fully analyzed both the posterior and left lateral images, with the three structuring elements having a new height of 200 pixels and a radius of 1 pixel. The results for both views are shown in Table 4.1 below.

Table 4.1: Morphological filtering and projection results with $\pm20^0$ rotation: posterior view (top), and left lateral view (bottom)

Structuring Element	Correlation Coefficient	Standard error of estimate (pixels)
Diamond	0.49	61
Disk	0.54	59
Ball	0.55	58

Structuring Element	Correlation Coefficient	Standard error of estimate (pixels)
Diamond	0.51	44
Disk	0.53	43
Ball	0.66	39

We notice that for the posterior view, the projection approach produced a correlation coefficient that was much higher than the one calculated with the automatic thresholding approach (r=0.17). Furthermore, the standard error of estimate decreased to about 60, which was better than the 69 pixels obtained with automatic thresholding. For both views, a ball structuring element appeared to be the best choice for the structuring element. Therefore, we decided to use the ball structuring element in further simulations.

4.3.3 Polynomial Fitting Analysis

To further improve our projection method, we developed a new algorithm for selecting the optimal rotation angle. A second-degree polynomial curve was fitted through the widths calculated for each rotation angle within a range of $\pm 20^0$, and the angle corresponding to the minimum value of the parabola was selected as the optimal rotation angle (Figure 4.11).

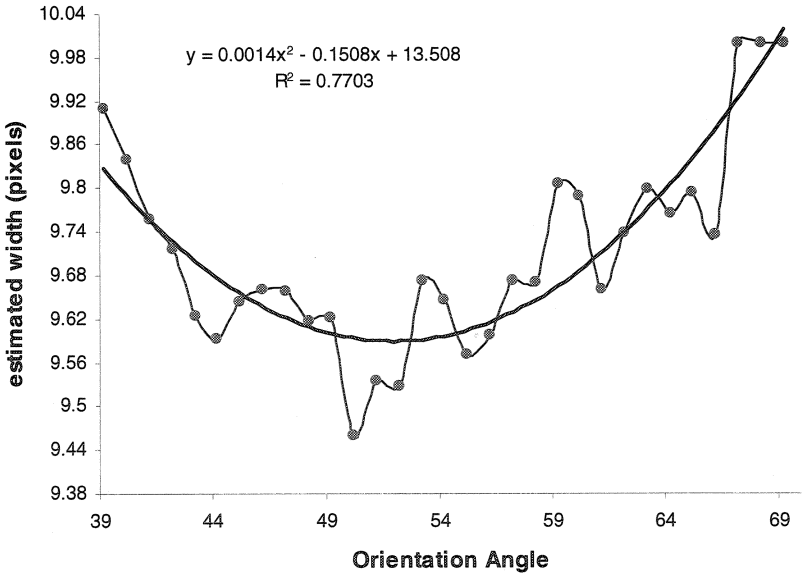

Figure 4.11 Polynomial curve fit through the estimated widths versus the projection angle

Polynomials in six images, out of the twenty posterior images, did not have a good fit or did not have a concave shape. The equation describing the polynomial was still calculated and a rotation value was still obtained. For the left lateral views, every image had a visible concave polynomial passing through the points. The correlation coefficient obtained in the posterior view analysis was r= 0.63 and the standard error of estimate was 56 pixels. For the left lateral views, the correlation coefficient was r= 0.58 and the standard error of estimate was 42 pixels. This is similar to results obtained with the previous rotation method with selection of the minimum width. However, we must consider the fact that six images gave a false estimate for this "best-fit" analysis for the posterior view. The left lateral images gave us a high correlation coefficient but with a larger standard error of estimate.

4.4 Quantifying the Position Error

After many attempts with different structuring elements, the best results obtained with the projection approach had correlation coefficients that were statistically significant (p<0.05) at r= 0.55 for the posterior view and r= 0.66 for the left lateral view. The standard error of estimate of the depth computed from the width was 58 pixels for the posterior view and 39 pixels for the left lateral view. For the posterior view, the width of the electrode projection ranged from 7.4 to 9.6 pixels with an average value of 8.5 pixels, whereas for the left lateral view, the measured electrode width ranged from 7.1 to 8.9 pixels with an average value of 8 pixels. Since the catheter diameter was 2 mm, this indicates that the standard error of estimate of the depth was about 15 mm for the posterior view and 10 mm for the left lateral view.

To more fully understand the significance of this 10 mm error, we would like to know what effect this has on the isochronal maps when the estimated depths are used to superimpose the isochronal maps over the fluoroscopic images. In order to visualize this effect, we reconstructed the convex hull using the estimated Y and Z depths respectively,

in terms of pixels, for both the left lateral and the posterior views. Once these were calculated, we had a new three-dimensional set of points and a modified convex hull was reconstructed. Then, we superimposed the 2D isochronal maps as previously described in Chapter 3.

For the left lateral view, we reconstructed a new Convex Hull by retaining the X and Z pixel values from the original analysis, and by changing the Y pixel values to the ones estimated from the width. The estimation of the depth Y, yielded a *SD*= 57 pixels. The isochronal map fused onto the left lateral fluoroscopic image (XZ plane) showed the significance of the estimated depth. The estimates of depth in the Y direction produced a change in the color code of the isochronal map. When compared to the original superimposed isochronal map we notice that three activation times are no longer visible (Figure 4.12 right). Those three activation times have been pushed further back on the Convex Hull and are no longer visible in the lateral view, simply due to their respective estimated depth calculation.

As expected, for the posterior view, the results were worse than for the left lateral view. The estimation of the depth Z yielded a *SD*= 103 pixels. Again, the poor quality of contrast in certain posterior images made it difficult to locate visually the end electrode. Once the end electrode was cropped into a small window for the projection analysis the structuring element was able to still produce a dark background, however there were less pixels making up the area of the electrode in a certain number of the images. This probably produced a small under-estimate of the depth along the Z-axis. With respect to the original isochronal activation map superimposed on the posterior fluoroscopic image we noticed that six activation times were no longer visible (Figure 4.13 right).

The large estimation errors calculated for both views showed a misrepresentation of the electrical activation on both the Convex Hull and the isochronal maps generated, and are an indication of how poorly the estimation analysis was for images with a low contrast.

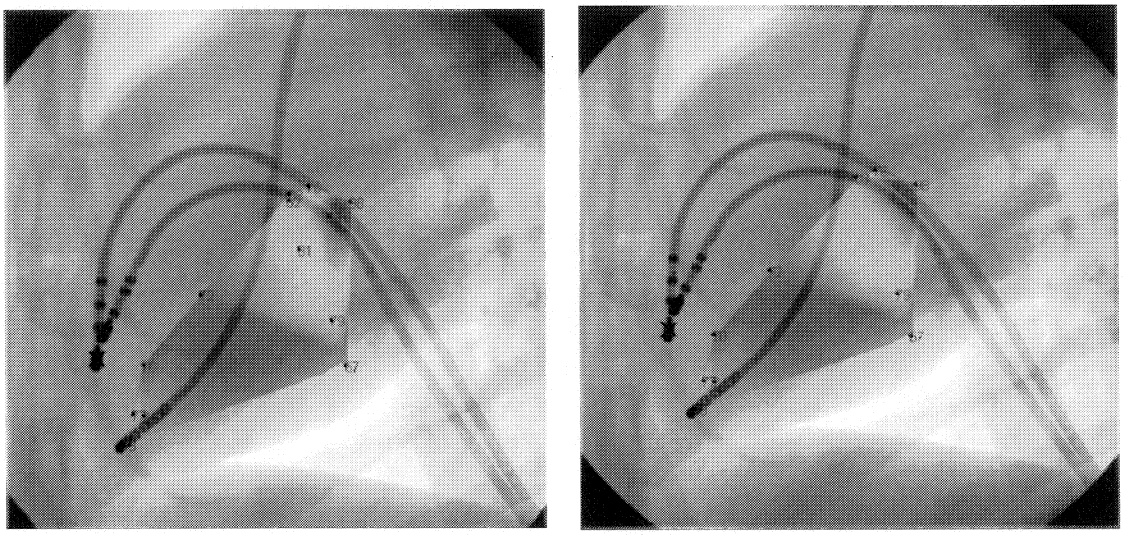

Figure 4.12 Left: Original isochronal map superimposed on the left lateral image. Right: New isochronal map, with 3 activation times no longer visible, computed with the estimated depth (Y).

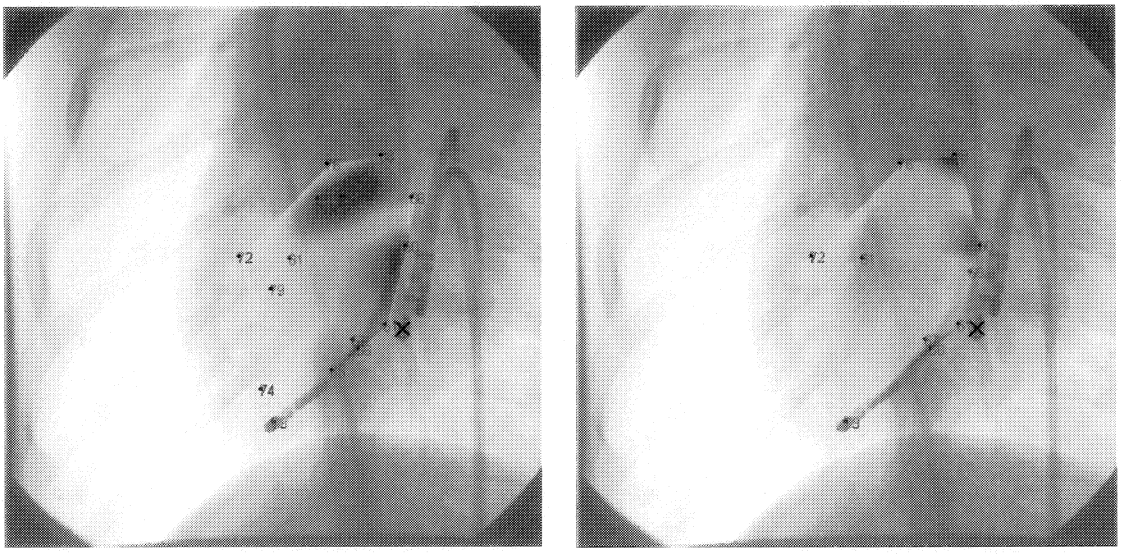

Figure 4.13 Left: Original isochronal map superimposed on the posterior image. Right: New isochronal map, with 6 activation times no longer visible, computed with estimated depth (Z).

Chapter 5

Discussion and Conclusions

We proposed different answers to the questions asked at the beginning of this work.

- To obtain 3D geometrical data about catheter locations from 2D images, we first used a biplane approach, then a monoplane approach.

  For the biplane analysis, we had to sequentially rotate the fluoroscope in order to acquire two perpendicular images. Once this was done, we calculated the 2D coordinates of the mapping catheter in each of the posterior and left lateral view images. Then, we assumed a true biplane setup and kept the X coordinate the same for both images in order to obtain the 3D XYZ positions of the catheters. The sequential measurements of the horizontal and vertical fluoroscopic images were not as accurate as simultaneous measurements with a true biplane fluoroscope as the vertical position of the reference catheter showed a small difference of 4±17 pixels in the 20 posterior and left lateral images. Motion artifacts such as respiration, subject movement and fluoroscope misalignment can explain this relatively small difference.

  For the monoplane analysis, we proposed two alternative approaches: the binary thresholding approach and the projection method with concurrent morphological filtering. Although the projection method yielded better depth estimates than the thresholding method, the results were disappointing since the standard error of estimate of the depth was too large for the construction of an accurate convex hull. The error was about 1.5 cm for the posterior view and about 1 cm for the left lateral view. Image contrast affects the accuracy of the depth estimates: visual analysis revealed that the left lateral images always had a better contrast than the posterior images because of the oblong section of the canine torso, and these left lateral images provided better depth estimates. We also found that electrode width could be overestimated because the tip electrode was superimposed over other objects in the

image (Figure 5.1). Therefore, at the outset of the experiment, vigilance should be exercised to position the catheter, as best as possible, to other locations away from the contours of the other catheters. Better image processing techniques remain to be developed in order to extract relevant 3D information from 2D fluoroscopic images for the monoplane approach.

Finally, we should mention that the images need not to be calibrated (with a grid or with autocalibration techniques) because there is no need to transform the pixel values of the image coordinates into millimeters of a "world" coordinate system since isochronal electrical activity maps are always plotted in the image coordinates for superposition with the fluoroscopic data.

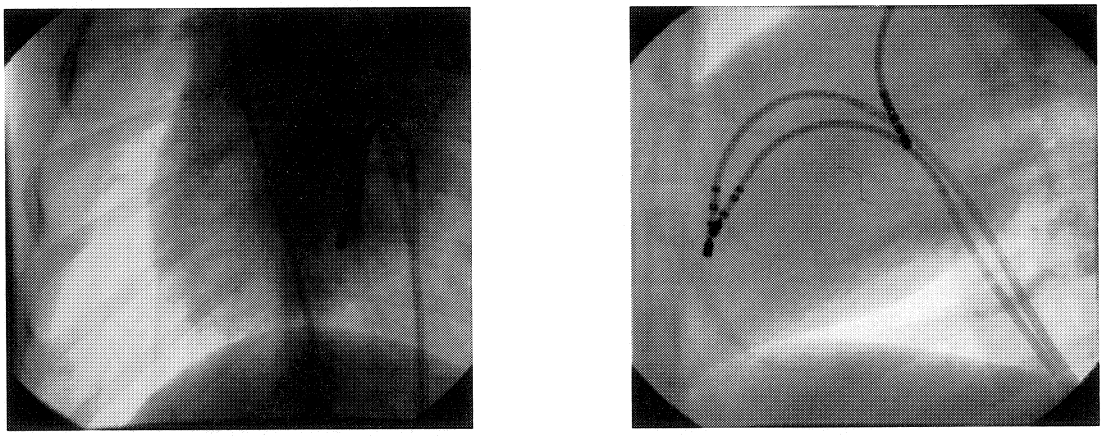

Figure 5.1 The mapping catheter in both images was positioned near or over the contours of the reference and pacing catheters. This leads to ineffective isolation of the catheter tip when applying the thresholding method or the projection method.

- To describe the geometry of the surface that encloses all the 3D electrode locations inside the cardiac chamber so that it can be visible from a specific vantage point, we investigated four approaches and finally selected the Convex Hull technique. This proved to be a good first choice. By retaining the normals from a certain point of view on the Convex Hull, two dimensional isochronal activation maps were superimposed over the corresponding fluoroscopic images. These isochronal maps

accurately depicted the progression of the electrical activation away from the pacing catheter. However, the endocardial surface is not a perfectly convex surface since 19 of our 20 endocardial mapping coordinates were located on the surface of the convex hull model, and other methods such as the Growing Cell Structures Approach should be investigated.

- To correct for motion artifacts due to the beating of the heart as well as the patient's respiration, we acquired the fluoroscopic images at the end of expiration and we used a reference catheter that was left in the right ventricle while we mapped the left ventricle with another catheter.
- Finally, we found that the proposed technique could be feasible in a clinical context only if the data is recorded with a biplane fluoroscopy system. For the biplane approach, we proposed a point-by-point method in order to obtain and superimpose effectively the isochronal maps onto fluoroscopic images. It would seem that by using standard equipment such as inexpensive catheters and our own personal data acquisition system, there is a strong possibility to simulate the function of the CARTO XP system, which is presently on the market, at a much lower cost. Our approach needs to be tested on human patients first. Also, data acquisition required approximately 30-40 minutes. Consequently, we can only target sustained, uniform arrhythmias with this approach.

Future perspectives

There is a real possibility in trying to investigate what effect a possible change in tip-electrode shape would have in our monoplane analysis. For instance, instead of applying the projection technique to the tip electrode, we can certainly isolate one of the smaller electrodes that lie near the catheter tip as well. These electrodes have a smaller rectangular shape and may be located in regions of better contrast. If this analysis provided better results, then the final analysis would have us calculate the distance from the smaller electrode to the tip electrode positioned on the endocardial surface. Once the

biplane and monoplane techniques are perfected, the auto calibration of the experimental scene is recommended in order to minimize distortions in the fluoroscopic images. This can be achieved using a calibration grid, with known spherical markers. The approach of Hartley and Anan [6] should be investigated in the context of isochronal fusion mapping.

REFERENCES

[1] SAVARD, Pierre, SIERRA, Gilberto, LeBLANC A., Robert, LEONARD Melanie, NADEAU, Reginald. September 2003. "Fluoroscopic Navigation System to Guide Catheter Ablation in cardiac arrhythmias. First Experiences." *Proc. XXV Conf. Of the IEEE Engineering in medicine and biology society. Cancun´03.* P. 138-142.

[2] NEITZEL, U. 2001. "X-Ray today." *Medica Mundi.* 45:3. 8-13.

[3] MORADY, F. 1998. "Radio-Frequency Ablation as Treatment for Cardiac Arrhythmias." *The New England Journal of Medicine.* 340:7. 534-544.

[4] VORPERIAN R., Vicken. April 2002. RF Ablation talk by Vicken R. Vorperian, M.D. with images from many sources. *Cardiac Radio Frequency Ablation Web Site-Publications.* [Online] http://rf-ablation.engr.wisc.edu./start_heart.html. (Page consulted on May 10, 2004.)

[5] THE MATHWORKS INC. 2003. Image Processing Toolbox: Image Analysis and Statistics. [Online]http://www.mathworks.com/access/helpdesk/help/toolbox/images/regionprops.html#254869 (Page consulted on June 21, 2004.)

[6] HARTLEY, R. and SILPA-ANAN, C. January 2002. "Reconstruction from two views using approximate calibration." *ACCV2002: the 5th Asian Conference on Computer Vision, Melbourne Australia.* 23-25.

[7] HEART DISEASE, CARDIOVASCULAR DISEASE RESOURCES. 2004. *Guidant Corporation, Illustrated Glossary.*

[Online].http://www.guidant.com/webapp/emarketing/compass/comp.jsp?lev1=resourc&lev2=glossary (Page consulted on May 10, 2004).

[8] WEBSTER G., John. 1998. *Medical Instrumentation: Application and Design*. 3rd ed. John Wiley and Sons Inc. 691p. Chapter 4.

[9] HEART DISEASE, CARDIOVASCULAR DISEASE RESOURCES. 2004. *Guidant Corporation, Tachycardias, Defibrillators and Heart Arrhythmias.* [Online]http://www.guidant.com/webapp/emarketing/compass/comp.jsp?lev1=tachy&lev2=causes. (Page consulted on May 10, 2004).

[10] HEART DISEASE, CARDIOVASCULAR DISEASE RESOURCES. 2004. *Guidant Corporation, Atrial Fibrillation.* [Online]http://www.guidant.com/webapp/emarketing/compass/comp.jsp?lev1=afib&lev2=glance. (Page consulted on May 10, 2004).

[11] HEARTCENTER ONLINE, FOR CARDIOLOGISTS AND THEIR PATIENTS. 2004. *Ablation (Radiofrequency Ablation, Catheter Ablation, Surgical Ablation, Radiofrequency Catheter Ablation, AV Node Ablation).* [Online]http://www.heartcenteronline.com/myheartdr/common/artprn_rev.cfm?filename=&ARTID=14. (Page consulted on May 10, 2004).

[12] EINTHOVEN: ADVANCES IN CARDIAC ARRHYTHMIAS. 2004. *Narrow-QRS tachycardias with regular rhythm.* [Online] http://www.xagena.it/einthoven/eint0138.htm. (Page consulted on May 10, 2004).

[13] GUPTA K., Anoop, MAHESHWARI, Alok, THAKUR, Ranjan, LOCKHANDWALA Y., Yash. 2002. "Cardiac Mapping: Utility or Futility." *Indian Pacing and Electrophysiology Journal.* 2:1. 20-32.

[14] ZIMMERMAN, Frank (M.D). 2001. "Advances in Catheter Ablation for the Treatment of Arrhythmias in Children." *Clinical Comment.* University of Chicago Medical Center. [Online] http://www.uchospitals.edu/pdf/uch_001078.pdf
(Page consulted on May 10, 2004).

[15] JOHNSON & JOHNSON GATEWAY. 2004. *CARTO XP EP Navigation System: Product information.*
[Online]http://www.jnjgateway.com/home.jhtml?page=viewContent&contentId=09008b988073dd83&loc=CAENG. (Page consulted on May 10, 2004).

[16] ENDOCARDIAL SOLUTIONS Inc. 2004. *Physician Information; Case Studies: Atrial Flutter.*[Online] http://www.endocardial.com/physician/atrial_flutter.html
(Page consulted on May 10, 2004).

[17] BOSTON SCIENTIFIC. 2004. *Electrophysiology Devices: Constellation Catheters.*
[Online]http://www.bostonscientific.co.uk/med_specialty/deviceDetail.jhtml?task=tskBasicDevice.jhtml&sectionId=4&relId=1,20,21,22&deviceId=490&uniqueId=MPDB273.
(Page consulted on May 10, 2004).

[18] SAVARD, Pierre. "Physiologie Cardio-Vasculaire: Du potentiel d'action à l'electrocardiogramme" *Notes de cours.* 2-8.

[19] TOET, D.J. March 2001. "A new vascular imaging system: the Integris Allura." *Medica Mundi.* 45:1. 2-9.

[20] SCHMIDT, P. September 1999. "From humble beginnings: the history of cardiac X-ray image management." *Medica Mundi*. 43:2. 10-15.

[21] SANTA, Muhammed. Fall 2003. "An Overview of 3D Photography and The Computational Aspect of Triangle Mesh" *Class Notes of Prof. Ioannis Stamos*, [Online] http://www.cs.hunter.cuny.edu/~ioannis/3DP_F03/mshanto/3D_project.pdf (Page consulted on May 5, 2004)

[22] NIENHUYS, Han-Wen, VAN DER STAPPEN, A. Frank. November 2002. *"A Delaunay approach to interactive cutting in triangulated surfaces."* Institute of Information and computing sciences, Utrecht University. 17p. Technical report # UU-CS-2002-044.

[23] SHEWCHUK, Jonathan R. May 1997. *Delaunay Refinement Mesh Generation.* 215p. Doctorate Thesis in Computer Science. Carnegie Mellon University.

[24] De BERG, Mark, VAN KREVELD, Marc, OVERMARS, Mark, SCHWARZKOPF, Otfried. 2002. *Computational Geometry: Algorithms and Applications*. Springer-Verlag. 367p. Chapter 9.

[25] AMENTA, Nina, BERN, Marshall, EPPSTEIN, David. March 1998. "The Crust and the β-Skeleton: Combinatorial Curve Reconstruction". *Graphical Models and Image Processing*.60/2:2. 125-135.

[26] AMENTA, Nina, BERN, Marshall, KAMVYSSELIS, Manolis. 1998. " A New Voronoi-Based Surface Reconstruction Algorithm". *Computer Graphics*. 32. 415-421.

[27] MENCL, Robert. 2001. *Reconstruction of surfaces from unorganized three-dimensional point clouds*. 196p. Doctorate Thesis in Field Information Technology, University of Dortmund, Germany.

[28] IVRISSIMTZIS, Ioannis, JEONG, Won-Ki, SEIDEL, Hans-Peter. 2003. Using Growing Cell Structures for Surface Reconstruction," *In Proc. Shape Modeling International*. 288. 78-88.

[29] BARBER, C. Barber., DOBKIN, P. David, HUHDANPAA, Hannu. 1996. The Quickhull Algorithm for Convex Hulls, ACM *Trans. Mathematical Software*. 22:4. 469-483.

[30] BOUDRY, C. 2002. Segmentations des Images. *Unité Régionale de Formation à l'Information Scientifique et Technique.*
[Online]http://web.ccr.jussieu.fr/urfist/image_numerique/segmentation.htm#seuil1
(Page consulted on May 12, 2004).

[31] OTSU, N. 1979. "A Threshold Selection Method from Gray-Level Histograms". *IEEE Transactions on Systems, Man, and Cybernetics*. 9:1. 62-66.

[32] FISHER, R., PERKINS, S., WALKER, A., WOLFART, E. 2003. Mathematical Morphology. *Hypermedia Image Processing Reference.*
[Online]http://homepages.inf.ed.ac.uk/rbf/HIPR2/matmorph.htm. (Page consulted on May 12, 2004).

[33] THE MATHWORKS INC. 2003. Image Processing Toolbox. Users Guide Version 4: Chapter 9. Morphological Operations.

[34] FISHER, R., PERKINS, S., WALKER, A., WOLFART, E. 2003. Mathematical Morphology: Dilation. *Hypermedia Image Processing Reference.* [Online]http://homepages.inf.ed.ac.uk/rbf/HIPR2/dilate.htm. (Page consulted on May 12, 2004).

[35] FISHER, R., PERKINS, S., WALKER, A., WOLFART, E. 2003. Mathematical Morphology: Erosion. *Hypermedia Image Processing Reference.* [Online] http://homepages.inf.ed.ac.uk/rbf/HIPR2/erode.htm. (Page consulted on May 12, 2004).

[36] FISHER, R., PERKINS, S., WALKER, A., WOLFART, E. 2003. Mathematical Morphology: Opening. *Hypermedia Image Processing Reference.* [Online] http://homepages.inf.ed.ac.uk/rbf/HIPR2/open.htm#1. (Page consulted on May 12, 2004).